Superthermal proton and electron fluxes in the plasma sheet transition region and their dependence on solar wind parameters

N.A. Stepanov[1,2], V. A. Sergeev[1], D.A. Sormakov[2], V. A. Andreeva[1], S. V. Dubyagin[3], N. Ganushkina[5], V. Angelopoulos[4], A. V. Runov[4]

1. St. Petersburg State University, St. Petersburg, Russia;
2. Arctic and Antarctic Research Institute, St. Petersburg, Russia;
3. Finnish Meteorological Institute, Helsinki, Finland;
4. University of California, Los Angeles, USA;
5. Department of Climate and Space Sciences and Engineering, University of Michigan, Ann Arbor, MI, USA

Correspondingauthor:Nikita Stepanov (nikitasa@aari.ru)

Key Points:

- Most important predictors of particle flux are Vsw and Ekl for electrons and Vsw and Pd (with smaller impact of Ekl) for protons
- Ekl time lags depend on energy and distance, with up to 24 hrs. lag (maximum value for present study) in the region closest to Earth
- Solar wind velocity controls the energetic population in the tail plasma sheet.

Abstract

To study further the factors and mechanisms controlling 10-150 keV particle fluxes in the inner magnetosphere, we investigate empirically their behavior in the nightside transition region (6-14Re) depending on solar wind (SW) parameters taken at different time lags. We aim to establish the hierarchy of predictors (V, N, Pd, Ekl=VByz $\sin^2(\theta/2)$ etc.) and the optimal range of their time delays, both depending on the distance and local time. We use THEMIS 5-min averaged observations of energetic proton and electron fluxes in 2007-2018 near the plasma sheet mid-plane and build regression models exploring the combination of predictors, taken at time delays up to 24hrs. The model obtained shows that protons and electrons are controlled differently by solar wind parameters: electrons are influenced equally by Vsw and Ekl, whereas protons are controlled mostly by Vsw and Pd, and less by Ekl. We found that a wide range of time delays is involved depending on distance and particle energy. Specifically, the Ekl affects the energetic fluxes with time delays up to 24 hrs. (or more), exhibiting the long delays in the innermost regions. As regards the mechanism of Vsw influence, the Vsw related flux changes are large and, to a large extent, established on the route of the energy flow from solar wind-to the plasma sheet and, eventually, the inner magnetosphere. We also identified a new parameter, NBL=VByz $\cos^2(\theta/2)$, which helps to reveal the loss processes in the plasma sheet transition region.

1 Introduction

Intense magnetospheric electric fields during, either large-scale convection or localized plasma injections, accompany transport of the energy and plasma from the plasma sheet into the inner magnetosphere (the radiation belt region), where the particles are further accelerated due to wave-particle interactions (Thorne et al., 2013). Important changes of magnetic field and particle characteristics occur at the transition between plasma sheet and inner regions, roughly between 6 and 15 Re on the nightside (later referred to as the plasma sheet transition region, PSTR), their plasma physics is not yet fully understood (e.g. Baumjohann et al., 1989; Espinoza et al., 2018; Miyashita et al., 2020). Our understanding would benefit from models which quantify the changes in the PSTR and determine the factors which control these changes. In this paper we focus on the superthermal plasma population (roughly for energies ranging from typical plasma temperature, a few keV, up to 100-200 keV) which feeds the ring current and provides the source population for high-energy particles in the radiation belt (Boyd et al., 2016). Our interest is different from models designed for direct, practical applications, we rather aim to reveal physical insight/information.

Motivated by space weather studies and observations during the Van Allen Probes mission era, a large number of empirical models have been suggested and analysis conducted during the last two decades to describe the plasma properties. These works use plasma sheet proton and electron moments (Tsyganenko and Mukai, 2003, Dubyagin et al., 2016; Wang et al., 2017), kappa distribution parameters (Espinoza et al., 2018; Stepanova et al., 2015; Wang et al., 2012), or superthermal particles with energies about hundred keV (Denton et al., 2019). Some models have also been built for electron fluxes with energies about few keV (Denton et al., 2016; Silanpaa et al., 2017), or up to few MeV at geostationary orbit (Kellerman et al., 2013; Simms et al., 2018; Boynton et al., 2013). Literature on MeV electrons at GEO is much more numerous but we

mention only a few examples because we are interested in a much lower energy range. Still, the overall picture appears to be incomplete and very fragmentary. Different authors explored different spatial domains, used different time resolutions, investigated different sets of controlling parameters (predictors) and used different tools/methods to build their models. Also the vast majority of models considered electrons and protons separately. Hence it is hard to compare these results and integrate them into one consistent picture. This challenge provides the motivation for our study.

There are a number of general guidelines we followed when designed our study. First, unlike of providing a prognostic model as many prior space weather-related studies did, we are rather focusing on a better understanding of the dynamical control of PSTR particle fluxes by the solar wind (SW) parameters. Second, contrary to prior studies we avoided using a mixture of solar wind and magnetospheric variables (AE, Dst, or ULF indexes) together in the list of potential predictors, because most of the latter ones depend on solar wind drivers which make their separation difficult. We do not deny a possibility to use both of them for prognostic purposes, but in this study we prefer to go as far as possible with initial (solar wind) drivers of activity. In our study we only consider the SW variables as input, but extend the analyses of parameters and of their time lags. Third, to obtain the model which allows us to quantify the importance of individual predictors in a transparent way, we utilize classic multiple regression analysis in a similar way to (Simms et al., 2018). Taking into account mutual correlations between input parameters allows an objective sequential grading of input variables and helps characterize quantitatively the relative importance of each predictor and their time lag.

As regards the choice of model input parameters, most previous studies consistently point towards the southward IMF, solar wind velocity (Vsw) and density (Nsw) the most efficient SW predictors of plasma sheet moments (Tsyganenko and Mukai 2003; Luo et al., 2011; Dubyagin et al., 2016; Wang et al., 2017, Boynton et al., 2013; etc.). However, the relative roles of these predictors differ for proton and electron moments. For example, at ~12Re proton temperature Tp, and pressure are mostly controlled by the SW pressure, whereas the electron temperature Te is also strongly affected by the substorm related parameters, which connected to southward IMF, such as AL index and SW reconnection electric field Ekl (Sergeev et al., 2015), which increase during periods of southward IMF. Another factor might be northward IMF, predictive importance of which was tested in Dubyagin et al., (2016). It is interesting that when considering energetic particle fluxes at the geostationary orbit (GEO), Vsw invariably appear among the most influential variables (e.g., Kellermann et al., 2011; Boynton et al., 2016; Simms et al., 2018). The specific mechanism(s) behind that Vsw control is still under discussion.

In contrast to magnetic activity indexes (e.g., Bargatze et al., 1985; Newell et al., 2007; etc.), the solar wind parameter influence on the PSTR population is not limited to a few hrs. long time window, but may extend to longer intervals, especially for PSTR particles in the high energy tail of energy spectrum. In fact, a number of studies have documented that MeV electrons at GEO respond best to SW variables with about 2 days delay, and that the SW density is as important predictor as velocity (e.g., Boynton et al., 2013, Simms et al., 2018). The different time delays and relative importance of SW predictors for different energies and species, and the dependence of these characteristics on whether the outer (plasma sheet) or inner (radiation belt) portions of the PSTR is evaluated, provide a challenge for such empirical study. A very large observational data base is necessary to discriminate between so many factors. The availability of continuous

solar cycle-long observations by three THEMIS spacecraft (Angelopoulos et al., 2008) orbiting on eccentric near-equatorial orbits (with apogees at 11-14 Re and orbital period ~24hrs) now enable us to consider this task.

In this paper we address the abovementioned problems by constructing an advanced empirical model of proton and electron temperature and fluxes of superthermal particles based on long-term THEMIS observations. We elect to construct models for particle fluxes at fixed energies rather than for the moments of Maxwellian or kappa distribution functions. This is because the spectra of protons and electrons consist of superposition of a few distinct energy populations which have different dynamical responses and thus may be subject to different control parameters (e.g., Wang et al., 2012; Walsh et al., 2020). Also, when different energy components have very different response time lags, models relying on moments are unsuitable: it was shown that moment-based models do not accurately predict the observed fluxes at fixed energies (Dubyagin et al., 2019).

In Section 2 we describe the observations and modeling approach, and illustrate our choice of time delay parameterization and the full set of 31 investigated predictors. In Section 3 we describe the model construction for our full region (6-14 Re, 18-24-06 hrs. MLT) using the entire database, thereafter referred to as the full model. We also identify the optimized set of 17 predictors which is then used in Section 4 to build region-binned models, in each of 9 regions restricted in radius and MLT. Overall performance of the model is discussed in Section 5. Discussion of our results and their possible interpretation is provided in Section 6.

2. Database and method
2.1. Observations

In this work we use electron and proton spectra from the ground moments product (GMOM L2) available at (http://themis.ssl.berkeley.edu/index.shtml), which combines the measurements made by the electrostatic analyzer (ESA, E ~ few eV – 30 keV) and the solid state telescope (SST, E ~ 25 keV – 6 MeV) aboard the THEMIS A, D and E satellites using high angular and energy resolution distribution functions when the spacecraft were operated in Fast Survey mode (Angelopoulos et al., 2008). By investigating the data quality, we faced a problem related to the very large dynamical range of energetic particle fluxes encountered at the PSTR. Specifically, the largest flux, often flagged as "saturated data" (flag=256, when the count rate exceeds 10^5), constitute roughly half of the data set in the PSTR. Nevertheless, we found that these data are scientifically useful because: (1) the flux values marked by this flag are not leveled off, but continue to increase when moving to closer distances; (2) the model of flux variation based on the extended data set (which includes "saturated data", but with spikes and other flagged data removed) showed significantly better results compared to the model which used only 'good data' (flag=0).Another important aspect is that, if using flag=0 data alone, we miss an important part of the parameter space corresponding to disturbed conditions. A more extended discussion of these issues is provided in Section 5 and Supplementary data.

We analyzed data in the central plasma sheet (CPS) at radial distances between 6 and 14 Re in the night sector (at SM longitudes between 90º and 270º) between 01 December 2007 and 31

December 2018. The CPS data were averaged on 5 min time intervals, each average representing one sample in our database. To select the CPS samples, we applied a composite criterion. For large distance range, R > 8 Re, the basic criterion was $\beta > 1$ but, in addition, we also allowed samples with low beta but $|Bn| > |Bt|$, where Bn and Bt are the normal and tangential magnetic field components in the local neutral sheet-related coordinate system, computed using the model of magnetospheric neutral sheet (Tsyganenko et al., 2015). This addition allows us to keep bursty bulk flow events, in which samples with $\beta < 1$ are occasionally encountered. For distances R < 8 Re where the equatorial magnetic field is strong and β alone is not that useful, we used $\beta > 1$ and either $|Bn| > |Bt|$ or Dn< 1Re, where Dn is the distance between the satellite and the modeled neutral sheet (Tsyganenko et al., 2015). The resultant data base array contains roughly about $5 \cdot 10^5$ 5 min CPS samples.

As we are mostly interested in the processes which form the source populations for the ring current and radiation belts, we chose as output parameters for our study the temperatures Tp, Te and the differential fluxes in the superthermal tail of particle distributions, namely, electron energy-fluxes at E= 10, 31 and 93 keV, and proton fluxes at E=34, 95 and 140 keV. The rationale behind this choice is that the lowest energy is comparable to the upper value of the temperature in the PSTR for each species, and that the energy range is about one decade. The conservative choice of upper proton energy was because for protons the amount of data above background at higher energy dropped considerably with increasing energy. Including temperatures Tp and Te also facilitates comparison of our results with previous statistical results, they are presented in Supplement.

Solar wind parameters at 5-min resolution were taken from the OMNI database (http://omniweb.gsfc.nasa.gov). Based on previous experience summarized in the Introduction, among potential predictors we use solar wind speed Vsw, density Nsw and flow dynamic pressure Pd. Instead of southward Bz we use the "dayside merging electric field" function Ekl = $V|Byz|\sin^2(\theta/2)$ (θ – is the angle between IMF and GSM Z-axis, IMF Byz = $(By^2 + Bz^2)^{1/2}$) which is a known driver characterizing the intensity of magnetospheric convection and resulting particle acceleration (Kan and Lee, 1979; Newell et al., 2007). However, small Ekl variation when ($\theta < 90$), due to small value of $\sin^2(\theta/2)$, lead to loss of information about northward IMF effects which also might have a predictive value (Dubyagin et al., 2016). We include information about northward IMF in the form of NBL = $|Byz|\cos^2(\theta/2)$. Unlike Ekl, NBL variations are higher during northward IMF. Time history of NBL may characterize the conditions without acceleration, with particle flux changes dominated by losses (which are typical for the inner magnetosphere, e.g., Forsyth et al., 2016). These parameters were averaged over the time bins selected at different lags as described below.

To analyze the spatial dependence of the solar wind control of the PSTR we divide the full area of interest into 9 sub-regions, as shown in Figure 1. Three azimuthal sectors, each 60º wide in SM longitude, allows us to reveal differences between dusk, midnight and dawn sectors. The inner radial distance bin (6 to 8 Re) characterizes the conditions in the outer radiation belt, whereas the outer bin (**10.5**-14 Re) corresponds nominally to the plasma sheet. It is our expectation that following the changes in these three radial bins can inform us about the transformation of particle fluxes during inward plasma convection. For each of the 9 sub-regions we build a corresponding regression model. Also, when investigating the regional and full

models, we use the radial distance (r) and SM longitude (φ or *long*) as predictor, so each regression model includes quantitative information about radial and azimuthal dependences.

2.2. Time delays

In prior linear models, it was customary to include the predictor values for different time lags as independent variables and then evaluate their efficiency by applying a statistical algorithm (see, e.g., Boynton et al., 2013; Simms et al., 2018;). Here we discuss how to optimize the choice of time delays of the predictors. If the number of time lag bins is too large the resolving power of the analysis would degrade. This number depends on the choice of both the time delay range and the width of averaging window.

Following Dubyagin et al., (2016), we evaluate the possible range of time delays with a correlation study, illustrated in Figure 2 for the "dayside merging electric field" Ekl predictor. Each point on the plot shows the color- coded Pearson correlation coefficient (CC) between the particular plasma sheet parameter and solar wind Ekl parameter. The plot shows the CC as a function of time window lag (T, on the X-axis) and window width (ΔT, on the Y-axis), both ranging between 0 and 24 hrs. (The time limit 24 hours was chosen for two reasons. First, most of the previous studies identified the primary response in this time domain for energies less than a hundred keV. Second, limiting the time range to <24h we avoid the possible influence of autocorrelation effects related to one-day orbital period of THEMIS satellite.) Different plots correspond to different distances in the nightside PSTR (top to bottom: R4, R5, R6) as well as to different PSTR parameters (left to right: Te, e31 or e93 ln(flux)). For electron temperature the peak correlation is found for ~2 hours delay (in agreement with previous analyses by Dubyagin et al., 2016; Sergeev et al., 2015), but it shifts toward the larger delays for the 31 keV and, especially, for 93 keV energy-fluxes. As a result, the lag patterns are highly different for Te and 93 keV flux. Another well-defined trend is the obvious increase of the time delay with decreasing radial distance, corresponding to the much longer delay (i.e. «solar wind memory») of energetic particle flux in the inner region compared to the PSTR's outer part.

We note that CC values in Fig.2 are low (~0.2) so these results alone cannot provide the full picture of optimal lags in the regression model. Nevertheless, these and similar plots constructed for other potential predictors help us to choose the range of possible time delays to be between 0 hr and 24 hrs. for the chosen output parameters. They also help us optimize the choice of time lag windows: by noticing that sensitivity of correlation to ΔT changes degrades as T increases, we may increase the window width proportionally to T, which helps to investigate large time lags interval with fewer of variables.

Finally, to investigate the time lags of the solar wind predictors affecting the plasma sheet parameters, each predictor (except for Vsw) is included in the model 7 times. Namely, they were averaged for the time periods which precede the plasma sheet observation by: 0-0.5, 0.5-1, 1-2, 2-4, 4-8, 8-16, 16-24 hours; such sequence is coded thereafter for the input parameter I as $I_{0/0.5}$, $I_{0.5/0.5}$, $I_{1/1}$, $I_{2/2}$, $I_{4/4}$, $I_{8/8}$ and $I_{16/8}$. As regards Vsw, it has a long autocorrelation time (44 hrs., Maggiolo et al., 2018) therefore it was accounted only once, taken the value at the time lags between 0.5 - 1 hrs. The full list of predictors, therefore, includes 31 parameters. Since the energetic particle fluxes strongly depend on the distance and MLT, besides solar wind

parameters we also include solar-magnetic(SM) coordinates (r, long) of THEMIS spacecraft into the set of predictors.

2.3. Regression analysis towards full model

We start from suggesting that particle energy flux J (or other magnetospheric variable, like Ti and Te) dependence on the values of n predictors P_i (i=1, n) can be described by the multiplicative form of power law dependencies, $J = C \, P_1{}^{a1} \times \ldots \times P_n{}^{an}$, where *C* and powers *a1*,…,*an* are the constants. After taking the logarithms we get the linear equation expressing the output variable *O (O = ln(J))* as a function of input variables Ii ($I_i = ln(P_i)$):

$$O = a_0 \; + \sum_{i=1}^{n} a_i I_i \qquad\qquad (1)$$

(In the model version shown below zero counts were excluded from data base, other ways of handling zeroes did not alter the modeling results) Based on that approach we build a series of linear regression models using ordinary least squares method for each particular plasma sheet parameters (energy fluxes or temperatures in PSTR) using regression equation (1).We note that regression coefficient a_i quantifies the contribution of particular predictor P_i to the output variable. Also the quantity $a_i \cdot \sigma_i$ where the σ_i is a standard deviation of a particular i^{th} parameter (I_i), helps evaluate the relative influence (later referred to as the weight) of that parameter in the model. We use "statmodels" python module (Seabold et al., 2010) to produce linear regression and other statistical computations.

To evaluate the efficiency of the resulting model we use Pearson correlation coefficient (CC), which shows the relationship between the relative variations of predicted and measured variables.

Some of the predictors in the initial data set may correlate with each other, resulting in multicollinearity in the predictors matrix. This makes the regression coefficient in the resulting model more unstable and harder to interpret. Like it was done in Simms et al., (2018), to identify intercorrelated predictors *Ii* we use variance inflation factor (VIF), given by equation (2).

$$VIF(I_i) = \frac{1}{1 - R^2_{I_i}} \qquad\qquad (2)$$

Here R^2 is the coefficient of determination (R-correlation coefficient in case of linear regression) between predictor I_i and all other predictors, based on their multiple-regression model (James et al., 2017). VIF detects multicollinearity in the set of predictors. Its minimum value (VIF = 1) means that the predictor does not correlate with other predictors. Its large values (say, VIF > 10) imply the multicollinearity, in that case the relative weight of a particular predictor is ill-defined and it cannot assist much to establish relative roles of the different predictors. The VIF factor alone cannot help to form the optimal data set of predictors which significantly influence the regression model. Starting to reject step by step the predictors having maximal VIFs we look at the behavior of model performance (CC) and stop the procedure when CC start to decrease.

We illustrate the usefulness of VIF-based reduction procedure for the full model which uses the entire database, that is, includes all subregions taken together. To minimize multi-collinearity in the predictors matrix, at each step we calculate VIF for each parameter, build the regression model (1) and compute CC. Then we repeat this process and on the next step we exclude the parameter which has the maximal VIF value. We continue until only THEMIS distance and longitude are left, this occurred at 30th iteration. Table 1 represents three particular steps (1st, 15th and 30th) of this iterative sequence. The name of each predictor (left column) includes the coded information about the corresponding time delay and averaging window (see 2.2, last paragraph). At the bottom of the table correlation coefficients for these three models are shown. The initial state, which includes the full set of parameters, is color-coded pink. Correlation here is around 0.8, although VIF can be as large as 82.46 for N 0.5/0.5 predictor, which will be rejected on the second iteration. After 15 iterations we obtained the green-colored column (in the middle of Table 1), where VIF does not exceed 2.46, whereas CC is almost unchanged compared to the iteration #1. According to Figure 3, further corrections noticeably decrease CC such that in this sense the green column represents an optimal set of predictors. The last (azure color) column shows the minimal model depending only on the spacecraft location (*r* and *long*). Its CC is considerably below those in the optimal set. In the following we use the models built for this optimal set of predictors (#15) to analyze the efficiencies of different predictors and different time delays.

3. The full model.

For the entire PSTR region (6-14Re, 90-270° SM Longitude) we build regression models of proton/electron fluxes at 34/95/140 keV and 10/31/93 keV energies, correspondingly, using the optimal predictor set discussed above. Summary for these models is presented in Table 2. Standard deviation and VIF of input variables are presented in columns *σ* and *vif,* correspondingly. The colored area displays regression coefficients *a*, together with their weights (*a•σ*) as commented below. Number of points included in regression analysis (*num*), *CC* of the resulted model is shown at the bottom. To compute from the model the energy fluxes at particular location in the PSTR and for particular solar wind conditions (characterized by the set of SW and position predictors P_i, i=1,17) one should use the formula $J = \exp[a_0 + \sum_{i=1}^{17} a_i * \ln(P_i)]$, with parameter values taken from corresponding columns in the table.

We remind that the weight *a•σ* provides another view on the predictor importance: it helps better estimate the relative influence of particular predictors on the range of output variations than **a** alone does. For example, whereas the a-coefficient of Vsw is an order of magnitude larger compared to the coefficients of a particular Ekl predictor in Table 2, terms of SW velocity is 4-6 times smaller than the σ of any Ekl predictor, which partly compensates the weight of Vsw compared to Ekl. The fields are color-coded according to the value of **a** and a•σ parameter to distinguish the most influential positive (red) and negative (blue) contributing predictors (> 0.1 in absolute magnitude); this assists the visual comparison of big tables constructed for many variables. Similar models were also built for proton and electron temperature; their corresponding tables can be found in the Supporting Information (Table S2).

Examining Table 2, we see that CC values in the full model are relatively high for energetic particle fluxes, namely 0.74 (for p-34keV channel), 0.75 (for p-95keV channel), 0.81 (p140),

0.80 (e31) and 0.86 (e93). These values are noticeably lower for 10 keV electrons (0.65), which may be related to their non-monotonic radial profile in the vicinity of their inner plasma sheet (Alfven) boundary. For the temperatures CC is also lower (0.66 for Te), especially for protons (0.48 for Ti) (Table S2). A local time asymmetry is also evident. It corresponds to expectations of particle acceleration by a duskward-directed convection electric field: both temperature and energetic particle fluxes increase from dawn to dusk for protons (coefficient against SM longitude - a<0; means i34/95/i140 increasing when SM long approaches dusk, 90°). Oppositely for electrons fluxes increase from dusk to dawn (a>0; means e10/e31/e93; increasing when long SM approaches dawn, 270°). The strongest impact on high-energy particle fluxes comes from their radial dependence (large negative a), which is well-known from previous studies (see e.g., Turner et al., 2012; Kistler et al., 2016). It is somewhat surprising that regression coefficient against r are positive for both Te and e10 flux; this may be related to the fact that inner plasma sheet boundary (and peak flux at these energies) occur in the middle of PSTR region (see e.g. Korth et al., 1999).

Regarding the solar wind parameters, an obvious leader (except for Tp parameter in PSTR, where Ekl has maximum a•σ = 0.07) is the solar wind velocity. Even taking into account a small range of relative Vsw variations, its a*σ exceeds (or is comparable to) the sum of a*σ corresponding to the next significant contributor which is Pd for protons and Ekl for electrons. This is consistent with most previous studies which invariably pointed out that the Vsw is among the most influential SW predictors for energetic particle fluxes (e.g. Kellerman et al., 2011; Boynton et al., 2013; Dubyagin et al., 2016; Sergeev et al., 2015; Wang et al., 2017). One way of electron energization can be the increase of chorus waves intensity in the inner magnetosphere during periods of high Vsw (Boynton et al., 2018; Simms et al., 2018).

On first glance, it is somewhat puzzling that solar wind flow pressure, the main SW force acting on the magnetosphere and the main predictor of pressure in the plasma sheet (Borovsky et al., 1998; Tsyganenko and Mukai 2003), plays such a minor role for energetic particle fluxes, especially for the electrons, although it was already alluded to before (Dubyagin et al., 2016; Sergeev et al., 2015; Wang et al., 2017). Significant flow pressure influence is only seen in mid-energy proton fluxes (p95 channel).

It is also puzzling that the main predictors are so different between proton and electron fluxes: the electrons are controlled by Vsw and Ekl, whereas the protons - by Vsw and Pd, with smaller Ekl effect, which is consistent with Sergeev et al., (2015). Vsw weight increases for the fluxes at higher energies. For electron 10 keV, 31 keV and 93 keV fluxes the Vsw weights are 0.34, 0.49 and 0.57 correspondingly. For proton 34, 95 and 140 keV fluxes they are 0.48, 1. and 1.

Ekl affects different parts of electron spectra with different time delays. For temperature Ekl shows the maximal contribution at 2-4 hrs. time lags; for 10, 31 and 93 keV fluxes, the maximal contribution comes from the wide window of 0.5-24 hrs., with a tendency of red area to shift to larger delays with the increasing energy. This is roughly consistent with indirect evidence provided by Boynton et al., (2016) and agrees with the Thorne et al., (2013) conclusion that more time is needed to produce electron fluxes of higher energy through multiple interactions with chorus elements. For protons Ekl-related flux increase peaked at time lag 2-4hrs is observed in

34/93 keV channels, but this effect fades away with increasing energy. Such time delay and energy range effects are consistent with substorm-related particle acceleration effects.

For proton temperature the Ekl weight is 2 times stronger than Vsw weight, the strongest Ekl effect is at 2-4 hour and 4-8-hour delay. For 95 keV fluxes Ekl effect (0.14) is weaker than Vsw (0.05) and have its maximum at 2-4 hour. delay. For delays larger than 16 hours Ekl weight becomes negative. This may be due to protons which are energized by substorms and move to the higher energy part of the spectra, decreasing fluxes at lower energies. Model of 140 keV fluxes shows similar ordering of the Ekl term weights (maximum at 2-4 hours, negative effect at 16-24 hours).

Two remaining predictors, Nsw and NBL, show systematically negative impact on the energetic particle fluxes. Both parameters affect more strongly the proton flux. Whereas Nsw correlates negatively with Vsw, its specific importance was previously noticed for the MeV electrons (Boynton et al., 2013). As regards NBL, for protons its influence is distributed over the large range of time delays, with indication that longer time delays >24h may contribute. For electrons the NBL effect peaks at 1-2h. These results will be later discussed in section 6.

4. Results of region-binned model.

To investigate in more details, the distance and local time dependence of solar wind control in the PSTR, we build the same regression model as before but separately for each of 9 spatial regions shown in Fig.1.The summary of resulting models is presented in Table 3 (and Table S3 for proton and electron temperatures), which contains 6 sub tables corresponding to different species and energies. The energy and species of modeled fluxes, together with the region names are shown at the top of each sub table; the number of data points, CC for each region is shown at the bottom. Here we show only the weights (a*σ) of each predictor with the color-coding similar to that in Table 2. One general change from full model (Table 2) to region-binned models is a general decrease of CC, mostly due to the decrease of the distance range and, consequently, of the variances of the particle flux, whose intensity strongly depends on distance.

The immediate conclusion from the comparison of Tables 2 and 3 is the general consistency of color patterns for particular parameters as well as their general stability between the regions. In particular, this implies that even, with ensembles roughly 10 times smaller than of the full model, regional models are still capable of reproducing the same behavior. As concerns the main findings of full model, in the regional models we again observe the superior role of Vsw predictor, the difference of predictor combinations which control proton and electron populations, a wide range of time lags of Ekl influence for electrons (0-24hrs) and mostly negative influence of SW density and NBL parameter on the energetic particle fluxes, with longer time delays for energetic protons than for electrons

Next there are a number of region-dependent features which we would like to point out. Three distance-dependent effects are evident. (1) With a few exceptions, the **V**sw weight is smaller in magnitude in the inner bins (R1, R4, R7) compared to the plasma sheet bins. (2) In the similar way, the Ekl influence on energetic particle fluxes drops down in the inner region for both

protons and electrons. The relative change between inner and outer shells is larger for Ekl than for Vsw, so in the inner region Vsw-related variations dominate over all other effects.(3) A noticeable distance-related time delay patterns are observed for 31 and 93 keV electrons in the nightside and morning sectors (R4-R6 and R7-R9, correspondingly), in which the time lag of response peak (value of $a*\sigma$ parameter) progressively increases from outer to the inner portions of PSTR. As regards the NBL parameter, its influence is negligible in the inner shell. It is interesting that its cumulative effects (summed over all delays) seems to increase with the increasing distance.

The local time dependence, especially dawn-dusk flux asymmetry is of large interest as a possible indication of large-scale convection. For electrons, the impact of Ekl (which is a proxy for magnetospheric convection) is largest on the dawnside and is smallest on the duskside, being consistent with their acceleration in the dawn-to-dusk directed electric field. For protons the reverse pattern is expected but, surprisingly, this asymmetry is very weak.

5. Overall model performance

In Figure 4 we compare the energy fluxes predicted by full and region-binned models (on left and right sides correspondingly) with observed fluxes for 31keV electron flux (top) and 95keV protons (bottom). Color of each pixel corresponds to the number of observations in the data range it covers. Similar plots for other PSTR parameters can be found in Supplementary data. Such comparison provides us with a number of results. One of them is a crescent-shaped form of e31 peak flux distribution for the full model, with predicted flux tended to lay above the diagonal both in low and high flux regions. In high flux region such feature might potentially appear because of saturation of observed flux (because of using the 'saturated' (flag=256) data, see the Section 2.1). However, such feature is absent in the region-binned model, indicating that the most probable explanation of unusual shape is inability to approximate the strong flux variations (steep flux decrease in the outer radiation belt and more flat distribution in the plasma sheet) with one power law exponent, as used in full model. Another striking feature is the banded pattern of proton fluxes in low flux region on the bottom plots, which is related to discreteness at low count rate levels (in the first decade). It introduces a noise in the proton data which explains lower CC for protons compared to electrons in Tables 2 and 3. Removal of banded area from the data set would eliminate such noise, but simultaneously the dynamic range of flux changes would shrink twice, which has a negative effect on the model performance.

The CC values for combined region-binned model (including all subregion models) are summarized in Table 4. In spite of the abovementioned data problems, our relatively simple linear regression approach, is able to rise the CC by roughly 0.2-0.3 for electrons (and by 0.1-0.2 for protons) compared to the models used only spatial variables. The correlation approaching the level around CC~0.8. The CC values are best for highest energy particles (e93 and p 140), and degrade with decrease of particle energy. Overall this is a rather good result which confirms, that even with relatively simple regression model, based on solar wind predictors taken at wide range of time delays between 0 and 24hrs, one may significantly improve the prediction of energetic particle fluxes in the PSTR region.

6. Discussion and concluding remarks.

The regression model in our study was aimed to evaluate and compare quantitatively the impacts of various solar wind predictors. It is based on medium time resolution (5 min) observations in the PSTR and solar wind, describes the superthermal PSTR population for both protons and electrons, includes a wide range of possible time delays (between 0 and 24h) and allows us to estimate quantitatively the relative impacts of solar wind predictors at different time lags. The nightside plasma sheet transition region between 6 and 14Re is an important domain at the interface between plasma sheet and radiation belt/ring current regions, where the plasma sheet population is processed by several physical mechanisms (convection and substorm-related plasma injections, wave-particle interactions, losses due to magnetic drifts and precipitation etc.) to feed the inner magnetosphere. Its inherent complexity is evident in the different importance of particular predictors and time lags for different plasma components, i.e., for its different energies and species (protons and electrons). The comparisons with published results made in Sections 3, 4 showed consistency with previous studies; below we discuss physical implications of the results obtained.

In the plasma sheet and PSTR the temperature and energetic particle flux increase toward the Earth which are understood as a result of betatron/Fermi acceleration during sunward magnetospheric convection and substorm injections in the magnetotail (Baumjohann et al., 1989; Borovsky et al., 1998; Tsyganenko and Mukai 2003; Espinoza et al 2018). The dawn-dusk asymmetry in Ti is not significant in the plasma sheet tailward of 10Re (Tsyganenko and Mukai 2003) but it is clearly observed in the inner region (at r<10 Re, Dubyagin et al.2016), with proton (electron) energy flux increasing toward dusk (toward dawn) as a result of particle magnetic drift in dawn-dusk directed convection electric field (see a discussion and comparison to simulation results in Wang et al., (2012). The radial and azimuthal dependences expected account for a considerable part of the particle flux variations as quantitatively presented in Tables 2 and 3 (Tables S2 and S3 for temperature).

The solar wind predictor Ekl, associated with dayside merging electric field, is known to be causally related to enhanced magnetospheric convection (e.g. Troshichev and Janzura 2006; Newell et al. 2007). Its action on the energetic particles is not limited to the immediate response to the convection enhancement which responds to southward IMF driver with a time lag up to a few hours (e.g. Bargatze et al., 1985; Weimer et al., 2011). Surprisingly, the efficiency of Ekl during the preceding hour (see e.g. the line for Ekl_0.5/0.5 in Table 2) is actually minor compared to that over longer time lags. The impact of Ekl lagged by 2-4 hrs. (Ekl_2/2 line), which can be associated with substorm effects, provides the largest impact for both Te and all electron and proton channels. For energetic electrons the longer time history is of large importance. Particularly, the peak impact of Ekl on 93 keV electrons is observed for time lag between 8 and 16 hrs. (line Ekl_8/8), and significant contributions are also seen for 16-24 hrs. window (and possibly for even longer time delays which were not tested in our study). This significance of time history much longer than on substorm scale is now recognized as the cumulative effect of multiple interactions of electrons on closed drift shells with chorus wave elements, allowing the particles to be accelerated to very high energies (e.g. Thorne et al., 2013). Particularly, this effect was previously discussed in relation to the production of a few MeV

electrons at GEO which includes time lags up to >2 days (Boynton et al., 2013, Simms et al., 2018).

Our results confirm this by showing that Ekl has a long-lasting effect on electrons. Its most effective time lags increase with the increase of electron energy up to 8-24 hrs. time lags for 93 keV electrons, (see Fig.2 and Table 2). The dawn-dusk asymmetry of the region where large time delays are observed for electrons (they are especially strong in the midnight and dawnside sectors in the outer PSTR portion, Table 3), is consistent with the action of dawn-dusk E-fields which accelerates electrons toward dawn combined with the asymmetry of chorus wave distribution peaked on night and dawn sectors (Gao et al., 2014;).

The weakness of Ekl-related asymmetry for energetic protons (see Table 3) is a surprising observation; it may partly be explained by the compensating effect of duskside magnetospheric field depression related to the partial ring current (e.g., Tsyganenko and Andreeva, 2015). This depression deforms the particle drift-shells, moving them closer to Earth at dusk compared to dawn. In the presence of a negative radial gradient of energetic particle flux this would cause the observed flux decrease at dusk. This effect adds to the acceleration-related asymmetry for electrons, but compensates it in case of protons. These qualitative considerations should be quantitatively investigated in future studies.

Whereas dayside reconnection and the Ekl parameter are mostly controlled by the southward IMF Bz component, northward IMF Bz (NBZ) effects also have been discussed, mostly in relation to the plasma sheet density changes (Terasawa et al., 1997; Tsyganenko and Mukai 2003; etc.). The mechanism behind that may include diffusion from tail flank to its center in the quiet-time magnetotail which brings cold and dense plasma into the tail center on relatively large time scale, about 6-12 hrs. (e.g., Terasawa et al., 1997; Li et al., 2008; etc.). A similar time scale of this effect may be expected for protons and electrons. As concerns, the NBL effects on CPS temperature, previously (Tsyganenko and Mukai 2003) failed to find any influence on the protons, and Dubyagin et al., (2016) found a very modest influence on PSTR electrons. At the same time, the drop of energetic ion flux on the closed field lines in the night side during northward IMF was also demonstrated in Kronberg et al., (2015) and Luo et al., {2017). Neither publication discussed its origin.

In our study we tested this effect by using the NBL parameter. Both full and regional models consistently show a noticeable decrease of particle flux and temperature as well as consistent patterns of their spatial, species and energy dependence. This effect is not so pronounced in the innermost area near, GEO (R1, R4, R7 –Table 3). Also it is weaker in the temperature but more evident in the energetic particle fluxes. As Table 2 nicely shows, the time delays are species-dependent, the efficient time lags for protons are distributed over the large range of time delays (with indication that time lags >24h may also contribute), whereas for electrons the NBL effect peaks at 1-4 hrs. time lag. These big differences between time lags of protons and electrons suggests that some other mechanism, besides the diffusive penetration of cold/dense plasma, should be invoked to explain the NBL effect. A plausible explanation includes the particle losses which are velocity dependent and, therefore, qualitatively match the observed species-dependent time lag differences (longer time lags for protons which have smaller velocity than electrons have). As regards the scattering mechanism, for protons the inner boundary of non-adiabatic

pitch-angle scattering in curved magnetic field stays always Earthward of ~8Re in any conditions (e.g., Lvova et al., 2005; Yue et al., 2014), and the isotropic proton precipitation persistently depletes the outer portion of the PSTR. As concerns electrons, conditions of this non-adiabatic scattering mechanism may occasionally occur near midnight at roughly r>10-12Re, so some other pitch-angle scattering mechanisms may need to be invoked to account for losses in the inner region. Particle losses may provide the negative change in the energetic particle flux during quiet conditions when there is no particle acceleration and, we postulate, this is what is revealed by using the NBL parameter in our modeling.

Finally, we discuss the solar wind velocity predictor, whose influence on temperature and energetic particle flux is superior to all other solar wind parameters in both inner and outer parts of PSTR region. Although its importance has been amply discussed in prior works (see, e.g., Borovsky et al., 1998; Tsyganenko and Mukai 2003, Kellermann et al., 2011, Boynton et al., 2013; Denton et al., 2018; Simms et al., 2018; Luo et al., 2011; Sergeev et al., 2015; Dubyagin et al., 2016), the physical mechanisms explaining its action and efficiency were not fully identified yet. There are at least two channels of Vsw influence. The first is that high speed solar wind is typically hot and tenuous, quite different from cold and dense slow wind (e.g., Xu and Borovsky, 2015). After passing through the bow shock, magnetosheath and magnetopause (see, e.g., investigation of Tp and Te changes in Wang et al. 2012), it results in a hot/tenuous population in the plasma sheet which is very different from cold/dense plasma under slow wind. Therefore, under high Vsw conditions the plasma sheet attains high temperature and larger energetic particle flux of both protons and electrons, as systematically observed at different distances in the plasma sheet (Borovsky et al., 1998; Tsyganenko and Mukai 2003; Dubyagin et al., 2016).

In addition, both high Te and low Ne values enhance the efficiency of additional particle acceleration. Particularly, this is true for the field-aligned electron acceleration where the field-aligned electric potential drop is proportional to $Te^{1/2}/Ne$ for the given field-aligned current density (Knight 1973).As regards the cyclotron instability (Thorne et al., 2013), its efficiency depends on the ratio of electron densities Nh/Nc (with Nh and Nc corresponding to hot electrons resonating with waves and background cold electron density which is close to total Ne) and recently (Gao et al., 2014) presented some observational evidence for that. We may notice that Ne ~ Nc and that a number of hot electrons, Nh, increases together with the Te increase, so the acceleration efficiency may increase with the growth of Te/Ne. In both abovementioned accelerations mechanisms, we also expect an increase of precipitated electron energy flux with increasing of Vsw and such dependence is really strong (Sergeev et al., 2018).

The second possible channel of Vsw influence on acceleration is the possible enhancement of dawn-dusk convection. Indeed, statistical analysis of DMSP E-field observations showed that, in addition to the IMF-dependent term, the cross-polar cap potential drop also includes the Vsw^2-related term (Boyle et al., 1997) of 10-40 kV interpreted as a manifestation of viscous-like interaction at the magnetopause. An important detail is that in cases of either electron precipitation (Sergeev et al., 2018) or cross-tail potential drop (Boyle et al., 1997), the Vsw-dependent term enters additively to the effects of Ekl, that is, to the effect of dayside merging-controlled convection. All this evidence points to Vsw-dependent energization which affects proton and electrons independently of the reconnection process operating in the magnetotail.

To visualize what our results can add to this discussion, we plotted in Figure 5 the median values of electron 31 keV fluxes (top) and of 95 keV proton fluxes (bottom) as a function of SM-longitude in the magnetotail (midnight is at 180°) separately for different distances in the plasma sheet, that is roughly along the trajectories of magnetic particle drift. The left and right plots are for two different Vsw intervals, 300-400 km/s and 500-700 km/s, the Ekl values in both cases are fixed for 1-2 hours lag in the narrow interval 0.6-0.9 mV/m, corresponding to the medium activity. We focus on the dawn-dusk asymmetry which may characterize the action of large-scale convective E-field in the PSTR. The asymmetry is significant for electrons and much weaker for protons, especially for slow solar wind. Weak asymmetry of energetic protons for the quiet magnetosphere was also observed by Kronberg et al., (2015). The absence of asymmetry was related to the transient localized dynamical processes in the magnetotail that are not necessarily associated e.g. with substorms (Grigorenko et al., 2013; Luo et al., 2014). Whereas the asymmetry is much larger for electrons than for protons, for each species the relative changes between dawn and dusk are of roughly the same magnitude when comparing slow and fast solar wind plots. The changes of electric field between these groups, therefore, are not that significant to provide the difference between fluxes in the left and right plots. It is also noteworthy that both electron and proton fluxes show a local maximum slightly pre- midnight, in the sector where the bursty bulk flows and particle injections are known to occur most frequently (Gabrielse et al 2014). These maximum is more intense for the fast solar wind periods, but for slow solar wind it is also observable.

However, the largest difference between slow/fast solar winds is in the general level of fluxes, this difference is especially large in the most distant PSTR portion, about a factor of ~5 larger for electrons and about a factor of ~80 larger for protons in the fast wind. The flux differences between two groups in the inner shell are smaller (factor of ~ 2 and 5), but still they are very pronounced. Previously a strong Vsw control of >38keV electron flux at distances up to 30 Re in the tail plasma sheet was shown by Luo et al (2011). Taking into account that sunward convection and bursty bulk flows bring particles inward on the nightside (Hori et al., 2000) the huge change of energetic particles flux in the plasma sheet at the entry to the PSTR is, undoubtedly, the main reason of superior Vsw impact on the energetic particle fluxes in the inner magnetosphere, with acceleration in the inner region playing possibly some additional role. A more accurate estimation of relative efficiency of these factors would require analysis and modeling of phase space densities in realistic magnetic fields (Turner et al., 2012), which is beyond the scope of this study.

Shortly summarizing the main physical findings of this modeling study we conclude that:
- There are obviously two main solar wind drivers (Vsw and Ekl) responsible for the flux increase of 10-200 keV energetic particles in the PSTR. Whereas different states of solar wind characterized by Vsw, control the energetic tails of plasma distributions populating the plasma sheet from outside, its further acceleration is controlled by Ekl via the enhanced convection and related secondary acceleration mechanisms;
- We find further indications that losses are important in PSTR, whose action is especially pronounced during quiet times (NBL effect) in the absence of significant acceleration;
- We got clear evidence supporting a long memory of past solar wind in the fluxes of 10-150 keV particles, whose duration noticeably increases with particle energy; namely, the memory of Ekl-related acceleration continues to be visible up to 24h (limit of our study) in

the studied energy range. This can be understood as an effect of delayed and distributed-in-time multiple-step acceleration related to convection surges and associated secondary mechanisms including wave-particle accelerations etc.

Acknowledgements.

References

Angelopoulos, V. (2008). The THEMIS mission. Space Science Reviews, 141, 5–34. https://doi.org/10.1007/s11214-008-9336-1

Artemyev, A. V., Vasko, I. Y., Lutsenko, V. N., Petrukovich, A. A. (2014), Formation of the high-energy ion population in the earth's magnetotail: spacecraft observations and theoretical models, 32, 1233– 1246, doi:10.5194/angeo-32-1233-2014.

Bargatze, L. F., D. N. Baker, R. L. McPherron, and E. W. Hones Jr. (1985), Magnetospheric impulse response for many levels of geomagnetic activity, J. Geophys. Res., 90(A7), 6387–6394, doi:10.1029/JA090iA07p06387.

Baumjohann, W., Paschmann, G., & Cattell, C. A. (1989). Average plasma properties in the central plasma sheet. Journal of Geophysical Research, 94(A6), 6597–6606. https://doi.org/10.1029/JA094iA06p06597

Borovsky, J. E., M. F. Thomsen, and R. C. Elphic (1998), The driving of the plasma sheet by the solar wind, J. Geophys. Res., 103(A8), 17617–17639, doi:10.1029/97JA02986.

Boyd, A. J., Turner, D. L., Reeves, G. D., Spence, H. E., Baker, D. N., & Blake, J. B. (2018). What causes radiation belt enhancements: A survey of the Van Allen Probes Era. Geophysical Research Letters, 45, 5253–5259. https://doi.org/10.1029/2018GL077699

Boyd, A. J., Spence, H. E., Huang, C-L., Reeves, G. D., Baker, D. N., Turner, D. L., Shprits, Y. Y. (2016). Statistical properties of the radiation belt seed population. Journal of Geophysical Research: Space Physics, 121, 7636–7646. https://doi.org/10.1002/2016JA022652

Boyle, C. B., Reiff, P. H., and Hairston, M. R. (1997), Empirical polar cap potentials, J. Geophys. Res., 102(A1), 111– 125, doi:10.1029/96JA01742.

Boynton, R. J., M. A. Balikhin, D. G. Sibeck, S. N. Walker, S. A. Billings, and N. Ganushkina (2016), Electron flux models for different energies at geostationary orbit, Space Weather, 14, doi:10.1002/2016SW001506.

Boynton, R., Balikhin, M., Billings, S., Reeves, G., Ganushkina, N., Gedalin, M., et al. (2013). The analysis of electron fluxes at geosynchronous orbit employing a NARMAX approach. Journal of Geophysical Research: Space Physics, 118, 1500–1513. https://doi.org/10.1002/jgra.50192

Boynton, R. J., Aryan, H., Walker, S. N., Krasnoselskikh, V., &Balikhin, M. A. (2018). The influence of solar wind and geomagnetic indices on lower band chorus emissions in the inner magnetosphere. Journal of Geophysical Research: Space Physics, 123, 9022–9034. https://doi.org/10.1029/2018JA025704

Denton, M. H., M. G. Henderson, V. K. Jordanova, M. F. Thomsen, J. E. Borovsky, J. Woodroffe, D. P. Hartley, and D. Pitchford (2016), An improved empirical model of electron and ion fluxes at geosynchronous orbit based on upstream solar wind conditions, Space Weather, 14, 511–523, doi:10.1002/2016SW001409.

Denton, M. H., Taylor, M. G. G. T., Rodriguez, J. V., & Henderson, M. G. (2019). Extension of an empirical electron flux model from 6 to 20 Earth radii using Cluster/RAPID observations. Space Weather, 17, 778– 792. https://doi.org/10.1029/2018SW002121

Dubyagin, S., N. Y. Ganushkina, I. Sillanpää, and A. Runov (2016), Solar wind-driven variations of electron plasma sheet densities and temperatures beyond geostationary orbit during storm times, J. Geophys. Res. Space Physics, 121, 8343–8360, doi:10.1002/2016JA022947.

Dubyagin, S., Ganushkina, N. Y., &Sergeev, V. A. (2018). Formation of 30 keV proton isotropic boundaries during geomagnetic storms. Journal of Geophysical Research: Space Physics, 123, 3436–3459. https://doi.org/10.1002/2017JA024587

Dubyagin, S., Ganushkina, N., & Liemohn, M. (2019). On the accuracy of reconstructing plasma sheet electron fluxes from temperature and density models. Space Weather, 17, 1704–1719. https://doi.org/10.1029/2019SW002285

Espinoza, C. M., Stepanova, M., Moya, P. S., Antonova, E. E., & Valdivia, J. A. (2018). Ion and electron κ distribution functions along the plasma sheet. Geophysical Research Letters, 45, 6362– 6370. https://doi.org/10.1029/2018GL078631

Forsyth, C., Rae, I. J., Murphy, K. R., Freeman, M. P., Huang, C. L., Spence, H. E., et al. (2016). What effect do substorms have on the content of the radiation belts? Journal of Geophysical Research: Space Physics, 121, 6292– 6306. https://doi.org/10.1002/2016JA022620

Gabrielse, C., Angelopoulos, V., Runov, A., and Turner, D. L. (2014), Statistical characteristics of particle injections throughout the equatorial magnetotail, J. Geophys. Res. Space Physics, 119, 2512– 2535, doi:10.1002/2013JA019638.

Gao, X., Li, W., Thorne, R., Bortnik, J., Angelopoulos, V., Lu, Q., Tao, X., Wang, S. (2014). New evidence for generation mechanisms of discrete and hiss-like whistler mode waves. Geophys Res. Lett. 41 (14), 4805–4811.

Grigorenko, E. E., et al. (2013), Current sheet structure and kinetic properties of plasma flows during a near-Earth magnetic reconnection under the presence of a guide field, J. Geophys. Res. Space Physics, 118, 3265– 3287, doi:10.1002/jgra.50310.

Hori T, Maezawa K., Saito Y., Mukai T. (2000). Average profile of ion flow and convection electric field in the near-Earth plasma sheet. Geophysical Research Letters, 27, 1623-1626, https://doi.org/10.1029/1999GL003737

James, Gareth; Witten, Daniela; Hastie, Trevor; Tibshirani, Robert (2017). An Introduction to Statistical Learning (8th ed.). Springer Science + Business Media New York. ISBN 978-1-4614-7138-7.

Kellerman, A. C., Shprits, Y. Y., and Turner, D. L. (2013), A Geosynchronous Radiation–belt Electron Empirical Prediction (GREEP) model, *Space Weather*, 11, 463– 475, doi:10.1002/swe.20074.

Kellerman, A. C., Shprits, Y. Y., Makarevich, R. A., Spanswick, E., Donovan, E., & Reeves, G. (2015). Characterization of the energy-dependent response of riometer absorption. Journal of Geophysical Research: Space Physics, 120, 615–631. https://doi.org/10.1002/2014JA020027

Kennel, C. F. (1969), Consequences of a magnetospheric plasma, Rev. Geophys., 7(1, 2), 379– 419, doi:10.1029/RG007i001p00379.

Kistler, L. M., and Mouikis, C. G. (2016), The inner magnetosphere ion composition and local time distribution over a solar cycle, J. Geophys. Res. Space Physics, 121, 2009– 2032, doi:10.1002/2015JA021883.

Korth, H., Thomsen, M. F., Borovsky, J. E., and McComas, D. J. (1999), Plasma sheet access to geosynchronous orbit, J. Geophys. Res., 104(A11), 25047– 25061, doi:10.1029/1999JA900292.

Kronberg, E. A., Grigorenko, E. E., Haaland, S. E., Daly, P. W., Delcourt, D. C., Luo, H., Kistler, L. M., and Dandouras, I. (2015), Distribution of energetic oxygen and hydrogen in the near-Earth plasma sheet. J. Geophys. Res. Space Physics, 120, 3415– 3431. doi: 10.1002/2014JA020882.

Knight S (1973) Parallel electric fields. Planet Space Sci 21:741–750

Kan, J.R. and Lee, L.C. (1979), Energy coupling function and solar wind-magnetosphere dynamo. Geophys. Res. Lett., 6: 577-580. doi:10.1029/GL006i007p00577

Li, W., J. Raeder, M. F. Thomsen, and B. Lavraud (2008), Solar wind plasma entry into the magnetosphere under northward IMF conditions, J. Geophys. Res., 113, A04204, doi:10.1029/2007JA012604.

Luo B, Tu W, Li X, Gong J, Liu S, Burin Des Roziers E, Baker DN (2011) On energetic electrons (>38 keV) in the central plasma sheet: data analysis and modeling. J Geophys Res 116: A09220. doi:10.1029/2011JA016562

Luo, H., Kronberg, E. A., Grigorenko, E. E., Fränz, M., Daly, P. W., Chen, G. X., Du, A. M., Kistler, L. M., and Wei, Y. (2014), Evidence of strong energetic ion acceleration in the near-Earth magnetotail, Geophys. Res. Lett., 41, 3724– 3730, doi:10.1002/2014GL060252.

Luo, H., Kronberg, E. A., Nykyri, K., Trattner, K. J., Daly, P. W., Chen, G. X., Du, A. M., and Ge, Y. S. (2017), IMF dependence of energetic oxygen and hydrogen ion distributions in the near-Earth magnetosphere, J. Geophys. Res. Space Physics, 122, 5168– 5180, doi:10.1002/2016JA023471.

Lvova, E. A., Sergeev, V. A., &Bagautdinova, G. R. (2005). Statistical study of the proton isotropy boundary. AnnalesGeophysicae, 23, 1311–1316. https://doi.org/10.5194/angeo-23-1311-2005

Maggiolo, R., Hamrin, M., De Keyser, J., Pitkänen, T., Cessateur, G., Gunell, H., &Maes, L. (2017). The delayed time response of geomagnetic activity to the solar wind. Journal of Geophysical Research: Space Physics, 122, 11,109–11,127. https://doi.org/10.1002/2016JA023793

Miyashita Y., K. Seki, K. Sakaguchi, Y. Hiraki, et al (2020), On the Transition Between the Inner and Outer Plasma Sheet in the Earth's Magnetotail, Journal of Geophysical Research: Space Physics, 125, 4,

Pierrard, V., Lazar, M. Kappa Distributions: Theory and Applications in Space Plasmas. Sol Phys 267, 153–174 (2010). https://doi.org/10.1007/s11207-010-9640-2

Newell, P. T., Sotirelis, T., Liou, K., Meng, C.-I., and Rich, F. J. (2007), A nearly universal solar wind-magnetosphere coupling function inferred from 10 magnetospheric state variables, J. Geophys. Res., 112, A01206, doi:10.1029/2006JA012015.

Newell, P. T., Sotirelis, T., Liou, K., and Rich, F. J. (2008), Pairs of solar wind-magnetosphere coupling functions: Combining a merging term with a viscous term works best, J. Geophys. Res., 113, A04218, doi:10.1029/2007JA012825.

Seabold, Skipper, and Josef Perktold. Statsmodels: Econometric and statistical modeling with python." Proceedings of the 9th Python in Science Conference. 2010.

Sergeev, V. A., N. P. Dmitrieva, N. A. Stepanov, D. A. Sormakov, V. Angelopoulos, and A. V. Runov (2015), On the plasma sheet dependence on solar wind and substorms and its role in magnetosphere-ionosphere coupling, Earth, Planets and Space,67, 133, doi:10.1186/s40623-015-0296-x

Sergeev, V., N. Stepanov, Y. Ogawa, S. Kaki, K. Kauristie, Solar wind dependence of electric conductances and currents in the auroral zone, Journal of Atmospheric and Solar-Terrestrial Physics, 2017, ISSN 1364-6826, https://doi.org/10.1016/j.jastp.2017.07.006.

Simms, L., Engebretson, M., Clilverd, M., Rodger, C., Lessard, M., Gjerloev, J., & Reeves, G. (2018). A distributed lag autoregressive model of geostationary relativistic electron fluxes: Comparing the influences of waves, seed and source electrons, and solar wind inputs. Journal of Geophysical Research: Space Physics, 123, 3646–3671. https://doi.org/10.1029/2017JA025002

Sillanpää, I., Ganushkina, N. Y., Dubyagin, S., & Rodriguez, J. V. (2017). Electron fluxes at geostationary orbit from GOES MAGED data. *Space Weather*, 15, 1602–1614. https://doi.org/10.1002/2017SW001698

Stepanova, M., and E. E. Antonova (2015), Role of turbulent transport in the evolution of the κ distribution functions in the plasma sheet, J. Geophys. Res. Space Physics, 120, 3702–3714, doi:10.1002/2014JA020684.

Terasawa, T., et al. (1997), Solar wind control of density and temperature in the near-Earth plasma sheet: WIND/GEOTAIL collaboration, Geophys. Res. Lett., 24, 935–938, doi:10.1029/96GL04018.

Thorne, R. M., Li, W., Ni, B., Ma, Q., Bortnik, J., Chen, L., et al. (2013). Rapid local acceleration of relativistic radiation-belt electrons by magnetospheric chorus. Nature, 504(7480), 411–414. https://doi.org/10.1038/nature12889

Troshichev, O., Janzhura, A., and Stauning, P. (2006), Unified PCN and PCS indices: Method of calculation, physical sense, and dependence on the IMF azimuthal and northward components, *J. Geophys. Res.*, 111, A05208, doi:10.1029/2005JA011402.

Tsyganenko, N. A., and Mukai, T. (2003), Tail plasma sheet models derived from Geotail particle data, J. Geophys. Res., 108, 1136, doi:10.1029/2002JA009707, A3

Tsyganenko, N. A., Andreeva, V. A., and Gordeev, E. I.: Internally and externally induced deformations of the magnetospheric equatorial current as inferred from spacecraft data, Ann. Geophys., 33, 1–11, https://doi.org/10.5194/angeo-33-1-2015, 2015.

Tsyganenko N. A. and V. A. Andreeva (2015), A forecasting model of the magnetosphere driven by an optimal solar-wind coupling function, J.Geophys.Res., 8401–8425, DOI: 10.1002/2015JA021641

Turner, D. L., Angelopoulos, V., Shprits, Y., Kellerman, a., Cruce, P., & Larson, D. (2012). Radial distributions of equatorial phase space density for outer radiation belt electrons. Geophysical Research Letters, 39, L09101. https://doi.org/10.1029/2012GL051722

Walsh, B. M., Hull, A. J., Agapitov, O., Mozer, F. S., & Li, H. (2020). A census of magnetospheric electrons from several eV to 30 keV. *Journal of Geophysical Research: Space Physics*, 125, e2019JA027577. https://doi.org/10.1029/2019JA027577

Wang, C.-P., Gkioulidou, M., Lyons, L. R., and Angelopoulos, V. (2012), Spatial distributions of the ion to electron temperature ratio in the magnetosheath and plasma sheet, J. Geophys. Res., 117, A08215, doi:10.1029/2012JA017658.

Wang, C.-P., Kim, H.-J., Yue, C., Weygand, J. M., Hsu, T.-S., and Chu, X. (2017), Effects of solar wind ultralow-frequency fluctuations on plasma sheet electron temperature: Regression analysis with support vector machine, J. Geophys. Res. Space Physics, 122, 4210–4227, doi:10.1002/2016JA023746

Xu, F., and Borovsky, J. E. (2015), A new four-plasma categorization scheme for the solar wind, J. Geophys. Res. Space Physics, 120, 70–100, doi:10.1002/2014JA020412.

Yue, C., Wang, C.-P., Lyons, L., Liang, J., Donovan, E. F., Zaharia, S. G., and Henderson, M. (2014), Current sheet scattering and ion isotropic boundary under 3-D empirical force-balanced magnetic field, J. Geophys. Res. Space Physics, 119, 8202–8211, doi:10.1002/2014JA020172.
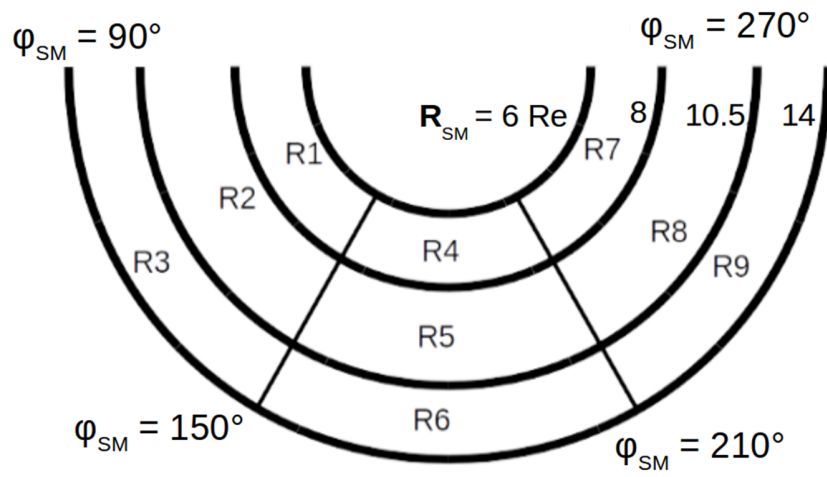
Figure 1. *Subregions used for region-binned regression model.*
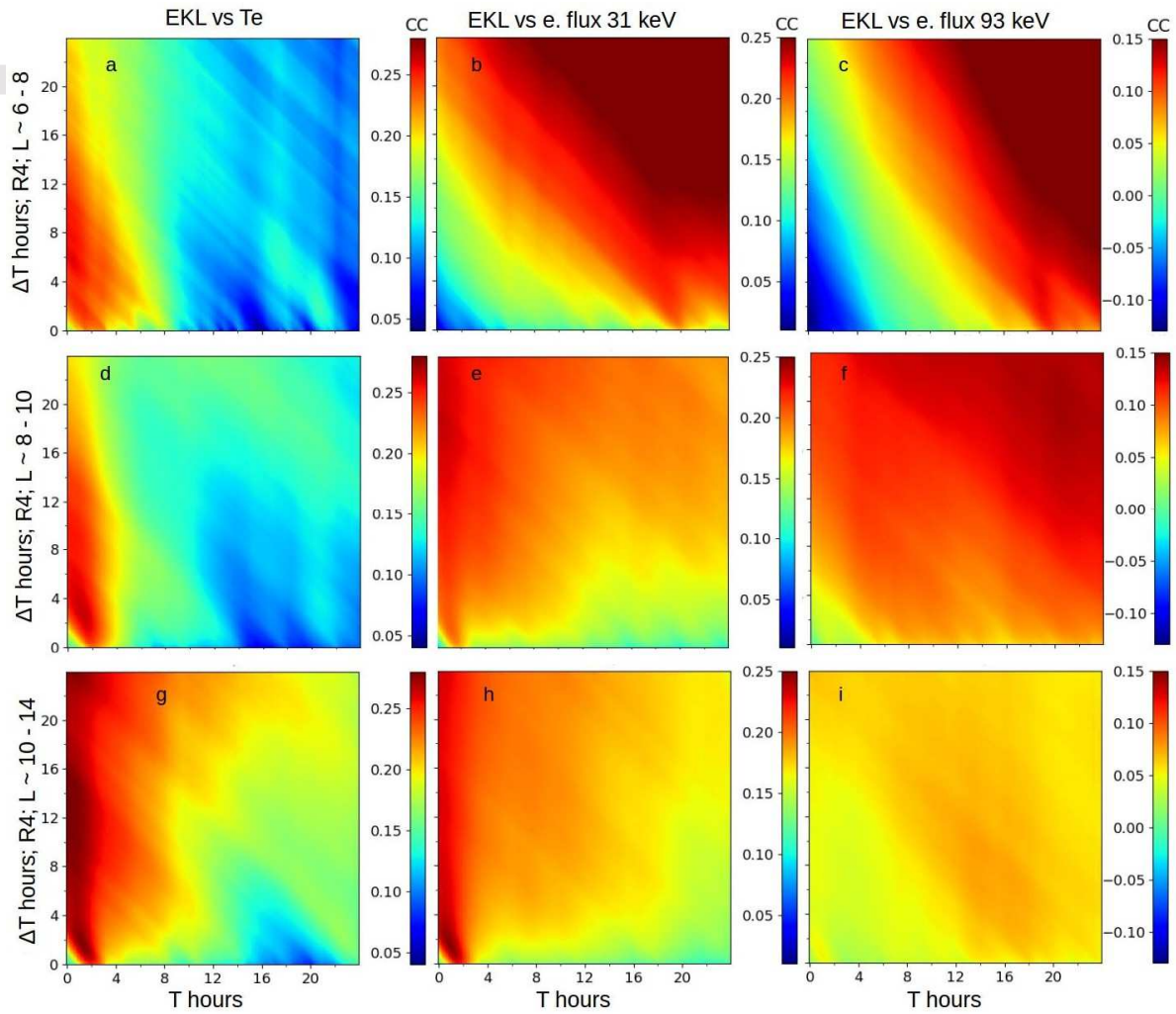
Figure 2. *Dependence of color coded Pearson correlation coefficients (see colorbar) between plasma sheet electron parameters (Te, e31 or e93) and the solar wind Ekl averaged over the preceding time interval between -(T+ΔT) and –T (T and ΔT are shown on horizontal and vertical axis correspondingly, time resolution is 5 minutes). Three horizontal rows correspond to three distances in the near-midnight PSTR sector, see Fig.1 for region coding scheme.*
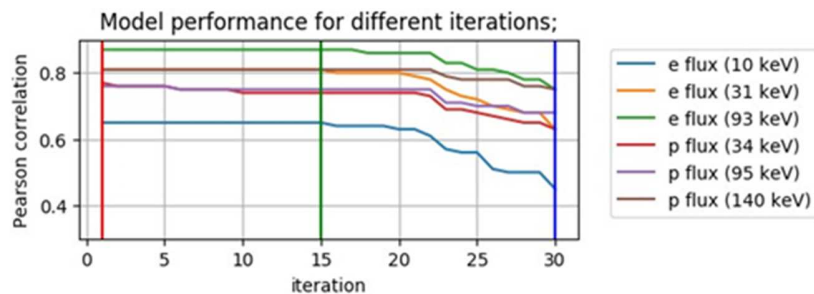
Figure 3. *Changes of model performance (CC) for particle fluxes at different energies (see legend) with increase of iteration number.*

Predicted vs observed energy fluxes
$$\log\left(eV*(s*cm^2*ster*eV)^{-1}\right)$$
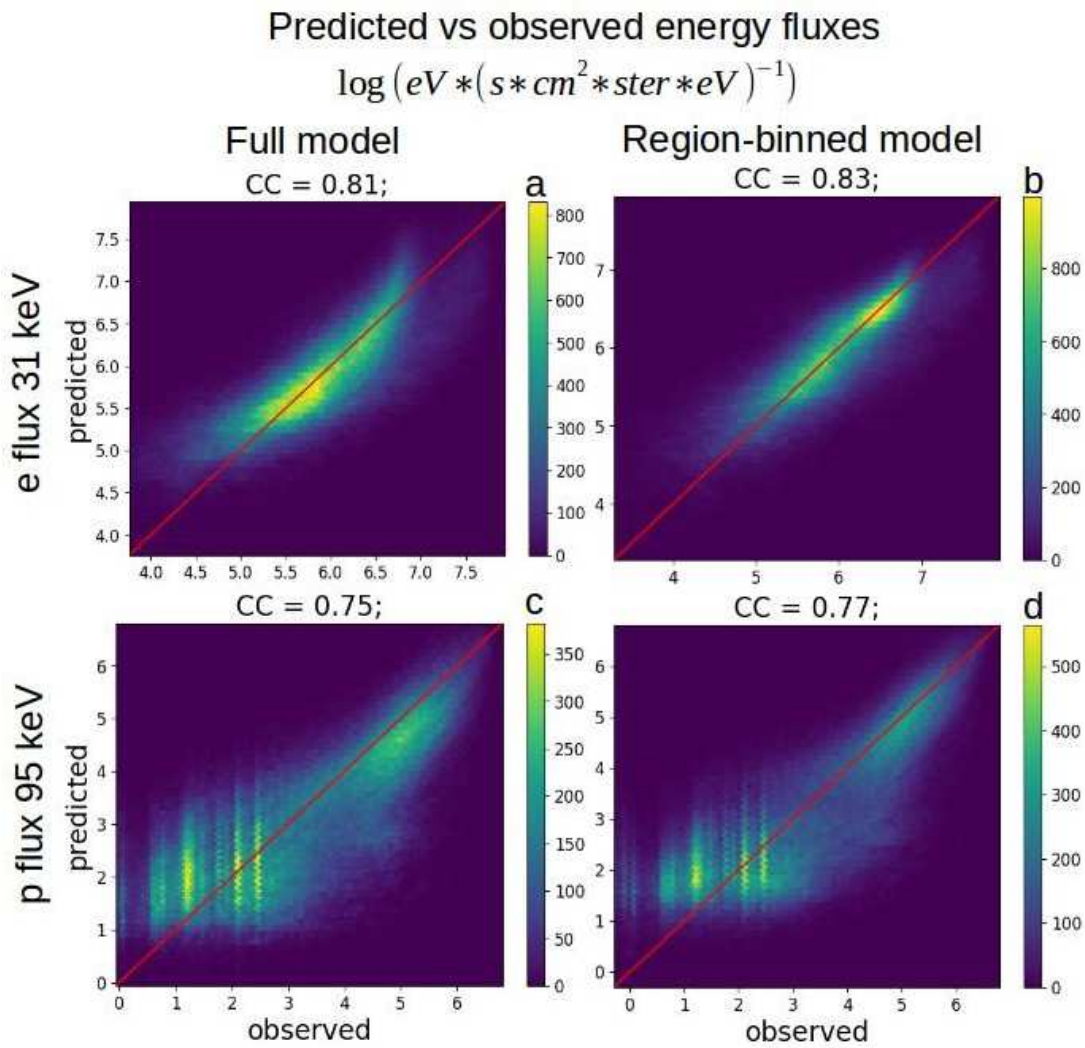
Figure 4. *Scatter plots of predicted versus observed energy flux values of 31 keV electrons (top) and of 95keV protons (bottom); color of each bin indicate the number of observations according to the color bar on the left side.*
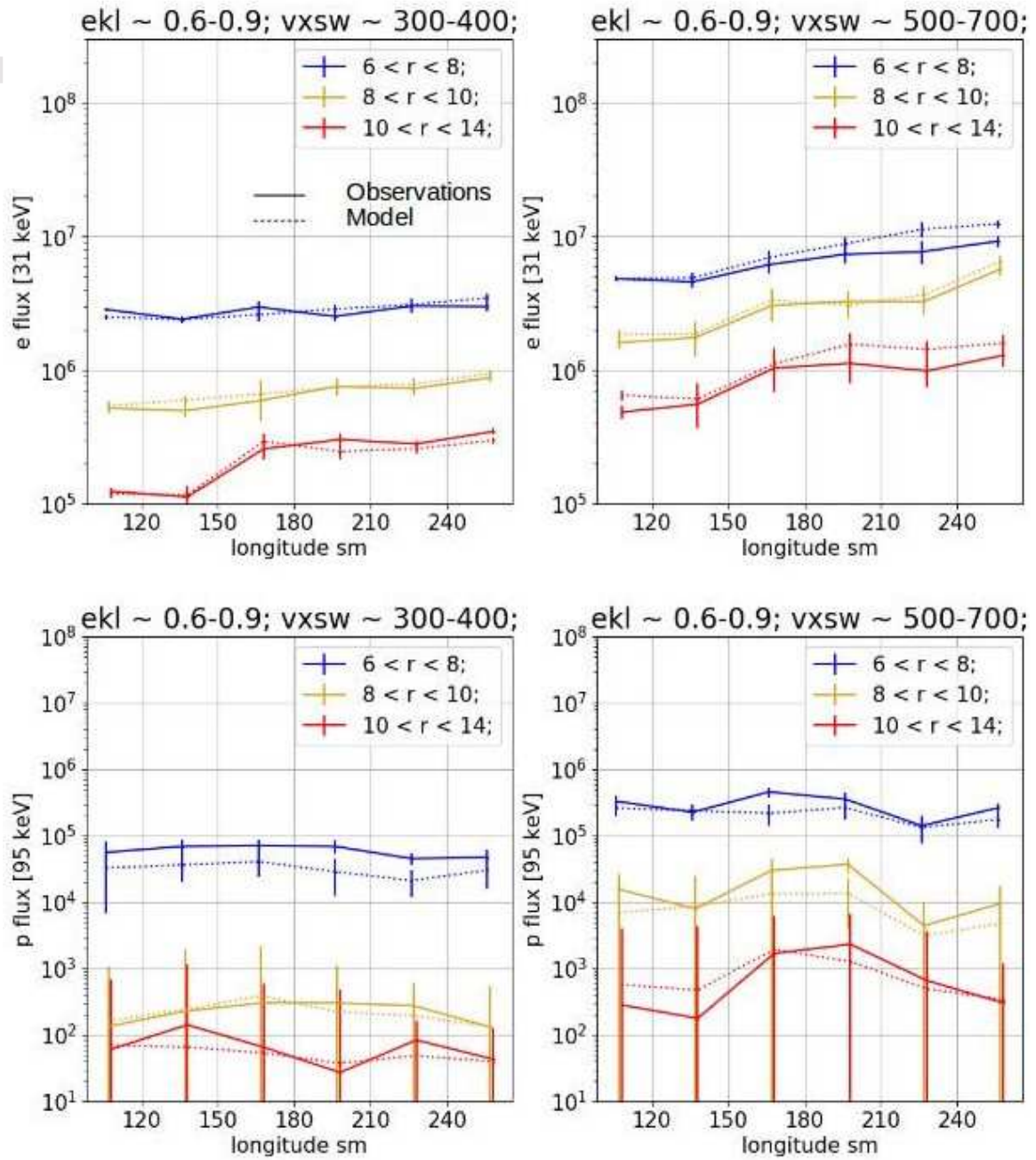
Figure 5. *Median values of 31keV electron fluxes (top) and 95keV proton fluxes (bottom)at different longitudes for two ranges of SW velocity (300-400 and 500-700 km/s) wind speed and under the same Ekl values (0.6-0.9 mV/m). Confidence Intervals (95% CI) are shown by vertical error bars.*

Iteration	1	15	30
Inputs T/ΔT hr	Varianceinflationfactor		
Vx 0.5/0.5	4,43	2,2	x
N 0/0.5	49,7	1,92	x
N 0.5/0.5	82,46	x	x
N 1/1	56,5	x	x
N 2/2	34,94	x	x
N 4/4	20,07	2,46	x
N 8/8	13,47	x	x
N 16/8	7,3	1,71	x
Pd 0/0.5	32,94	x	x
Pd 0.5/0.5	49,8	x	x
Pd 1/1	37,95	x	x
Pd 2/2	26,76	2,45	x
Pd 4/4	15,89	x	x
Pd 8/8	11,57	x	x
Pd 16/8	7,61	x	x
EKL 0/0.5	4,72	x	x
EKL 0.5/0.5	6,46	1,77	x
EKL 1/1	5,01	x	x
EKL 2/2	3,81	2,32	x
EKL 4/4	3,11	2,8	x
EKL 8/8	2,58	2,44	x
EKL 16/8	1,89	1,7	x
NBL 0/0.5	5,39	2,2	x

Iteration	1	15	30
Inputs T/ΔT hr	Varianceinflationfactor		
NBL 0.5/0.5	7,27	x	x
NBL 1/1	5,47	2,34	x
NBL 2/2	3,87	x	x
NBL 4/4	2,89	2,17	x
NBL 8/8	2,23	2,06	x
NBL 16/8	1,76	1,51	x
r	1,01	1,01	1
long	1,02	1,02	1
	Correlation(CC)		
e flux 10 keV	0,65	0,65	0,45
e flux 31 keV	0,81	0,81	0,63
e flux 93 keV	0,87	0,87	0,75
p flux 34 keV	0,77	0,74	0,63
p flux 95 keV	0,76	0,75	0,68
p flux 140 keV	0,81	0,81	0,75

Table 1.Results of initial (1), "optimal" (15) and final (30) iterations of the set correction algorithm. Top line shows the iteration number. First column shows the name of the predictor. 2nd, 3rd, 4th columns - VIFs of predictors for corresponding iterations. Bottom line: Correlation coefficient for the model at each iteration (see text for more details).

inputs (I) T/ΔT hrs.		# (i)	σ	vif	e flux 10 keV		e. flux 31 keV		e. flux 93 keV		p flux 34 keV		p flux 95 keV		p flux 140 keV	
Outputs (O) ->					a	a*σ	a	a*σ	a	a*σ	a	a*σ	a	a*σ	a	a*σ
const		0	\	\	-5,4		8,6		14,2		14,4		11,67		13,98	
Solarwind	Vx 0.5/0.5	1	0,22	2,2	1,53	0,34	2,23	0,49	2,59	0,57	2,16	0,48	4,56	1,00	4,55	1,00
	N 0/0.5	2	0,63	1,92	0,28	0,18	-0,06	-0,04	-0,15	-0,09	-0,05	-0,03	-0,18	-0,11	0,07	0,04
	N 4/4	3	0,62	2,46	0,01	0,01	-0,09	-0,06	-0,25	-0,16	-0,17	-0,11	-0,43	-0,27	-0,38	-0,24
	N 16/8	4	0,61	1,71	-0,08	-0,05	-0,05	-0,03	-0,19	-0,12	-0,08	-0,05	-0,16	-0,10	-0,41	-0,25
	Pd 2/2	5	0,53	2,45	0,07	0,04	-0,09	-0,05	-0,13	-0,07	0,12	0,06	0,31	0,16	0,08	0,04
	Ekl 0.5/0.5	6	1,47	1,77	0,10	0,15	0,02	0,03	-0,01	-0,01	0,03	0,04	-0,01	-0,01	0,01	0,01
	EKL 2/2	7	1,19	2,32	0,22	0,26	0,16	0,19	0,13	0,15	0,18	0,21	0,10	0,12	0,05	0,06
	EKL 4/4	8	1,03	2,8	0,16	0,16	0,15	0,15	0,13	0,13	0,13	0,13	0,02	0,02	0,00	0,00
	EKL 8/8	9	0,89	2,44	0,12	0,11	0,13	0,12	0,18	0,16	0,08	0,07	-0,03	-0,03	-0,01	-0,01
	EKL 16/8	10	0,91	1,7	0,10	0,09	0,11	0,10	0,14	0,13	-0,05	-0,05	-0,17	-0,15	-0,07	-0,06
	NBL 0/0.5	11	1,32	2,2	-0,03	-0,04	-0,02	-0,03	-0,02	-0,03	-0,01	-0,01	-0,01	-0,01	-0,02	-0,03
	NBL 1/1	12	1,23	2,34	-0,13	-0,16	-0,14	-0,17	-0,11	-0,14	-0,10	-0,12	-0,14	-0,17	-0,08	-0,10
	NBL 4/4	13	1,02	2,17	-0,06	-0,06	-0,14	-0,14	-0,12	-0,12	-0,06	-0,06	-0,10	-0,10	-0,07	-0,07
	NBL 8/8	14	0,87	2,06	-0,04	-0,03	-0,08	-0,07	-0,10	-0,09	-0,12	-0,10	-0,19	-0,17	-0,14	-0,12
	NBL 16/8	15	0,9	1,51	-0,01	-0,01	-0,03	-0,03	-0,05	-0,05	-0,14	-0,09	-0,22	-0,20	-0,18	-0,16
SM	r	16	0,2	1,01	0,44	0,09	-5,24	-1,05	-8,83	-1,77	-6,22	-1,24	-13,14	-2,63	-14,65	-2,93
	Long	17	0,34	1,02	2,2	0,75	0,82	0,28	0,52	0,18	-0,17	-0,06	-0,33	-0,11	-0,35	-0,12
	num	\	\	\	485900		485722		480117		485898		426794		426109	
	CC	\	\	\	0,65		0,81		0,87		0,74		0,75		0,81	

Table 2. *Results of the full model for the optimal set of predictors. See text for explanations.*

e flux 10 keV / p flux 34 keV

	Inputs T/ΔT hr.	e flux R1	R2	R3	R4	R5	R6	R7	R8	R9	p flux R1	R2	R3	R4	R5	R6	R7	R8	R9
Solar wind	Vx 0.5/0.5	0,22	0,31	0,37	0,55	0,37	0,41	0,67	0,35	0,16	0,33	0,63	0,58	0,29	0,38	0,79	0,26	0,48	0,53
	N 0/0.5	0,01	0,33	0,35	0,12	0,20	0,16	0,25	0,29	0,07	-0,01	-0,06	-0,06	0,06	-0,15	-0,06	0,02	0,10	0,04
	N 4/4	-0,08	0,01	-0,06	0,14	0,01	0,06	0,11	0,01	-0,05	-0,04	-0,05	-0,03	-0,11	-0,09	-0,17	-0,11	-0,15	-0,11
	N 8/4	-0,01	0,05	-0,05	-0,07	-0,02	-0,05	-0,04	-0,03	-0,06	-0,12	-0,15	0,04	-0,07	-0,13	0,01	-0,01	-0,01	0,01
	Pd 2/2	0,02	-0,07	0,10	0,04	0,08	-0,01	0,08	-0,04	0,04	0,07	0,03	-0,03	0,04	0,24	0,30	0,05	-0,01	-0,01
	Ekl 0.5/0.5	0,03	0,07	0,09	0,32	0,29	0,12	0,28	0,18	0,03	0,03	0,03	0,06	0,03	0,12	0,12	-0,04	0,00	0,03
	EKL 2/2	-0,13	-0,10	0,15	0,30	0,25	0,42	0,60	0,49	0,37	0,05	0,17	0,27	0,05	0,12	0,38	-0,01	0,18	0,38
	EKL 4/4	0,10	0,20	0,44	0,12	0,12	0,16	-0,06	0,05	0,16	0,02	0,11	0,12	0,00	0,10	0,14	0,06	0,16	0,31
	EKL 8/8	0,14	0,17	0,09	0,04	0,10	0,11	0,15	0,09	0,12	0,05	0,04	0,02	0,05	0,05	0,05	0,04	0,12	0,17
	EKL 16/8	0,13	0,05	0,03	0,19	0,09	0,07	0,15	0,10	0,06	0,01	-0,03	-0,12	0,02	-0,06	-0,16	0,05	0,02	-0,04
	NBL 0/0.5	-0,03	0,01	-0,07	-0,08	-0,07	-0,04	-0,05	-0,04	-0,03	0,00	-0,01	-0,11	-0,03	0,00	-0,05	-0,01	0,03	0,01
	NBL 1/1	0,06	0,01	-0,11	-0,32	-0,28	-0,23	-0,26	-0,17	-0,17	-0,01	-0,07	-0,21	-0,01	-0,14	-0,23	-0,01	-0,10	-0,20
	NBL 4/4	0,00	-0,03	-0,07	0,12	-0,06	-0,15	-0,09	-0,07	-0,11	-0,01	-0,11	-0,08	-0,05	-0,06	-0,13	-0,02	-0,05	-0,08
	NBL 8/8	-0,03	0,06	-0,14	-0,08	0,03	-0,04	0,01	-0,06	-0,01	-0,04	-0,11	-0,14	-0,02	-0,08	-0,13	-0,07	-0,12	-0,09
	NBL 16/8	-0,05	-0,07	-0,04	0,09	0,00	0,05	-0,05	0,05	-0,02	-0,03	-0,05	-0,14	-0,05	-0,05	-0,21	-0,05	-0,07	-0,10
SM	r	-0,23	0,42	-0,13	0,39	0,12	-0,51	0,57	-0,03	-1,05	-0,84	-1,22	-3,07	-0,83	-1,23	-2,45	-0,80	-1,34	-2,61
	Long	0,35	0,86	0,77	1,49	1,07	0,38	-0,50	0,00	0,36	0,02	-0,01	-0,02	-0,11	-0,15	-0,10	0,05	-0,12	-0,46
	num	38153	51724	72436	33628	42302	47082	38479	63723	98373	38153	51724	72436	33628	42302	47080	38479	63723	98373
	CC	0,38	0,43	0,63	0,61	0,61	0,67	0,71	0,66	0,6	0,65	0,61	0,55	0,59	0,61	0,65	0,64	0,63	0,62

e flux 31 keV / p flux 95 keV

	Inputs T/ΔT hr.	e flux R1	R2	R3	R4	R5	R6	R7	R8	R9	p flux R1	R2	R3	R4	R5	R6	R7	R8	R9
Solar wind	Vx 0.5/0.5	0,27	0,42	0,51	0,42	0,55	0,67	0,51	0,59	0,51	0,56	1,35	0,90	0,67	1,33	1,61	0,51	1,10	0,82
	N 0/0.5	-0,03	-0,04	-0,21	0,03	0,01	-0,06	0,04	0,08	0,02	-0,28	-0,30	-0,19	-0,06	-0,22	-0,07	-0,22	-0,03	-0,01
	N 4/4	0,01	-0,07	-0,04	-0,06	-0,08	-0,03	0,05	-0,12	-0,12	-0,28	-0,17	-0,13	-0,40	-0,39	-0,41	-0,23	-0,35	-0,16
	N 8/4	-0,07	-0,04	-0,05	-0,03	-0,06	-0,09	-0,01	-0,01	0,02	-0,39	-0,31	0,11	-0,25	-0,18	0,03	-0,30	-0,07	0,09
	Pd 2/2	-0,07	-0,12	-0,08	-0,06	-0,08	0,07	-0,01	-0,04	0,00	0,13	0,21	0,20	0,00	0,38	0,50	0,02	0,01	0,11
	Ekl 0.5/0.5	-0,07	-0,07	0,00	0,00	0,09	0,10	0,09	0,12	0,06	-0,06	-0,01	0,06	-0,10	0,07	0,06	-0,15	-0,01	-0,04
	EKL 2/2	0,08	0,17	0,27	0,07	0,10	0,27	0,10	0,17	0,29	0,00	0,18	0,18	-0,01	0,02	0,27	-0,02	0,10	0,25
	EKL 4/4	0,02	0,08	0,21	0,05	0,21	0,20	0,11	0,11	0,22	-0,03	0,00	-0,06	-0,14	0,09	0,07	0,00	0,08	0,10
	EKL 8/8	0,09	0,12	0,04	0,07	0,13	0,20	0,12	0,13	0,16	-0,04	-0,16	0,02	-0,06	-0,21	-0,03	-0,04	0,07	0,20
	EKL 16/8	0,08	0,08	0,05	0,12	0,10	0,09	0,15	0,10	0,10	-0,12	-0,14	-0,35	-0,07	-0,06	-0,44	-0,05	-0,05	-0,11
	NBL 0/0.5	0,03	0,00	-0,07	0,01	-0,04	-0,08	-0,05	-0,01	-0,03	-0,04	-0,05	-0,12	0,00	0,04	0,00	-0,09	0,05	0,03
	NBL 1/1	0,01	-0,01	-0,12	-0,07	-0,20	-0,33	-0,09	-0,22	-0,28	-0,05	-0,07	-0,31	-0,04	-0,22	-0,25	-0,05	-0,15	-0,25
	NBL 4/4	-0,05	-0,16	-0,16	-0,04	-0,14	-0,27	-0,05	-0,11	-0,18	-0,11	-0,24	-0,06	-0,21	0,02	-0,04	-0,09	-0,10	-0,04
	NBL 8/8	-0,02	-0,03	-0,15	-0,06	-0,06	-0,05	-0,01	-0,09	-0,09	-0,17	-0,18	-0,07	-0,13	-0,30	-0,17	-0,19	-0,22	-0,10
	NBL 16/8	-0,01	-0,05	-0,04	-0,01	0,01	0,01	-0,04	0,02	0,00	-0,12	-0,14	-0,23	-0,16	-0,23	-0,16	-0,42	-0,25	-0,23
SM	r	-0,64	-1,17	-1,70	-0,58	-1,11	-1,07	-0,40	-1,28	-1,40	-3,11	-2,43	-2,62	-3,18	-2,60	-1,73	-3,31	-2,69	-1,74
	Long	-0,10	-0,09	0,11	0,31	0,33	0,35	0,43	0,72	0,50	-0,20	-0,30	-0,10	0,04	-0,23	-0,06	0,54	-0,25	-0,81
	num	38129	51707	72414	33618	42297	47024	38479	63722	98332	37956	47111	56823	33416	40082	39045	38210	56474	77677
	CC	0,65	0,72	0,75	0,61	0,7	0,72	0,7	0,75	0,7	0,75	0,59	0,37	0,72	0,59	0,54	0,75	0,57	0,38

e flux 93 keV / p flux 140 keV

	Inputs T/ΔT hr.	e flux R1	R2	R3	R4	R5	R6	R7	R8	R9	p flux R1	R2	R3	R4	R5	R6	R7	R8	R9
Solar wind	Vx 0.5/0.5	0,34	0,51	0,72	0,46	0,53	0,79	0,45	0,56	0,66	0,58	1,08	0,60	0,82	1,46	1,38	0,67	1,23	0,90
	N 0/0.5	-0,08	-0,18	-0,25	-0,01	-0,03	-0,06	-0,06	-0,01	-0,03	-0,23	-0,33	-0,06	-0,01	0,03	0,16	-0,16	0,09	0,24
	N 4/4	-0,07	-0,16	-0,16	-0,16	-0,22	-0,10	-0,04	-0,24	-0,20	-0,32	-0,11	-0,14	-0,43	-0,51	-0,31	-0,25	-0,24	-0,06
	N 8/4	-0,18	-0,15	-0,13	-0,12	-0,16	-0,19	-0,11	-0,07	-0,04	-0,52	-0,45	-0,09	-0,40	-0,37	-0,09	-0,51	-0,32	-0,05
	Pd 2/2	-0,07	-0,13	-0,14	-0,11	-0,10	0,02	-0,05	-0,06	0,02	0,04	0,13	0,23	-0,10	0,17	0,13	-0,06	-0,14	0,02
	Ekl 0.5/0.5	-0,06	-0,04	-0,04	-0,07	0,03	0,07	-0,06	0,03	0,03	-0,04	0,01	0,09	-0,09	0,07	0,09	-0,13	0,04	0,01
	EKL 2/2	0,01	0,14	0,29	0,00	0,05	0,29	0,01	0,08	0,25	-0,02	0,14	0,11	-0,04	0,02	0,19	-0,04	-0,01	0,14
	EKL 4/4	0,01	0,07	0,20	-0,02	0,11	0,22	0,07	0,12	0,25	-0,04	-0,07	-0,03	-0,19	0,10	0,08	-0,04	0,03	0,06
	EKL 8/8	0,07	0,15	0,08	0,08	0,18	0,25	0,10	0,20	0,28	-0,04	-0,11	0,04	-0,08	-0,22	-0,02	0,00	0,12	0,17
	EKL 16/8	0,07	0,14	0,12	0,09	0,14	0,10	0,12	0,19	0,15	-0,08	-0,07	-0,15	-0,03	0,01	-0,14	-0,04	-0,05	-0,04
	NBL 0/0.5	0,03	0,04	-0,05	0,05	-0,01	-0,07	-0,03	-0,01	-0,04	-0,07	-0,03	-0,08	0,01	0,04	0,05	-0,15	-0,01	0,00
	NBL 1/1	-0,02	-0,05	-0,15	-0,04	-0,12	-0,23	-0,01	-0,12	-0,21	-0,10	-0,11	-0,18	-0,04	-0,10	-0,18	-0,01	-0,07	-0,11
	NBL 4/4	-0,03	-0,15	-0,14	-0,06	-0,15	-0,23	-0,05	-0,08	-0,18	-0,11	-0,18	0,04	-0,21	0,08	0,02	-0,11	-0,11	-0,03
	NBL 8/8	-0,04	-0,05	-0,15	-0,08	-0,07	-0,10	-0,04	-0,11	-0,08	-0,18	-0,12	-0,01	-0,18	-0,31	-0,05	-0,21	-0,10	-0,04
	NBL 16/8	-0,03	-0,04	-0,02	-0,04	0,02	-0,05	-0,10	-0,05	-0,08	-0,12	-0,05	-0,11	-0,23	-0,11	-0,18	-0,29	-0,26	-0,17
SM	r	-1,35	-1,98	-2,81	-1,42	-1,82	-1,82	-1,26	-1,95	-2,21	-3,80	-2,84	-1,52	-4,02	-2,79	-1,25	-4,15	-2,78	-0,86
	Long	-0,25	-0,26	0,15	0,05	0,06	0,49	0,55	0,36	0,00	-0,35	-0,32	-0,02	-0,07	-0,57	-0,29	0,57	-0,03	-0,23
	num	38127	51628	70057	33593	42207	46041	38458	63582	96424	37905	46625	59378	33391	39882	39307	38081	54783	76757
	CC	0,78	0,79	0,77	0,74	0,75	0,72	0,75	0,77	0,71	0,79	0,62	0,36	0,76	0,65	0,54	0,77	0,63	0,42

Table 3. *Similar to Table 2 but for region-binned model. The tables are presented separately for each magnetospheric variable, different columns in each table corresponds to different spatial region (see Figure 1 for region coding, R1, R4 and R7 are the innermost regions near GEO).*

Specie/energy keV	CC: region binned model (no SW parameters)
e flux 10 keV	0.71(0.45)
e flux 31 keV	0.83(0.63)
e flux 93 keV	0.89(0.75)
p flux 34 keV	0.77(0.63)
p flux 95 keV	0.77(0.68)
p flux 140 keV	0.84(0.75)

Table 4. *Summary of CC illustrating the performance of combined region-binned model. The values in parenthesis correspond to the model which depends only on spatial variables (r and long).*
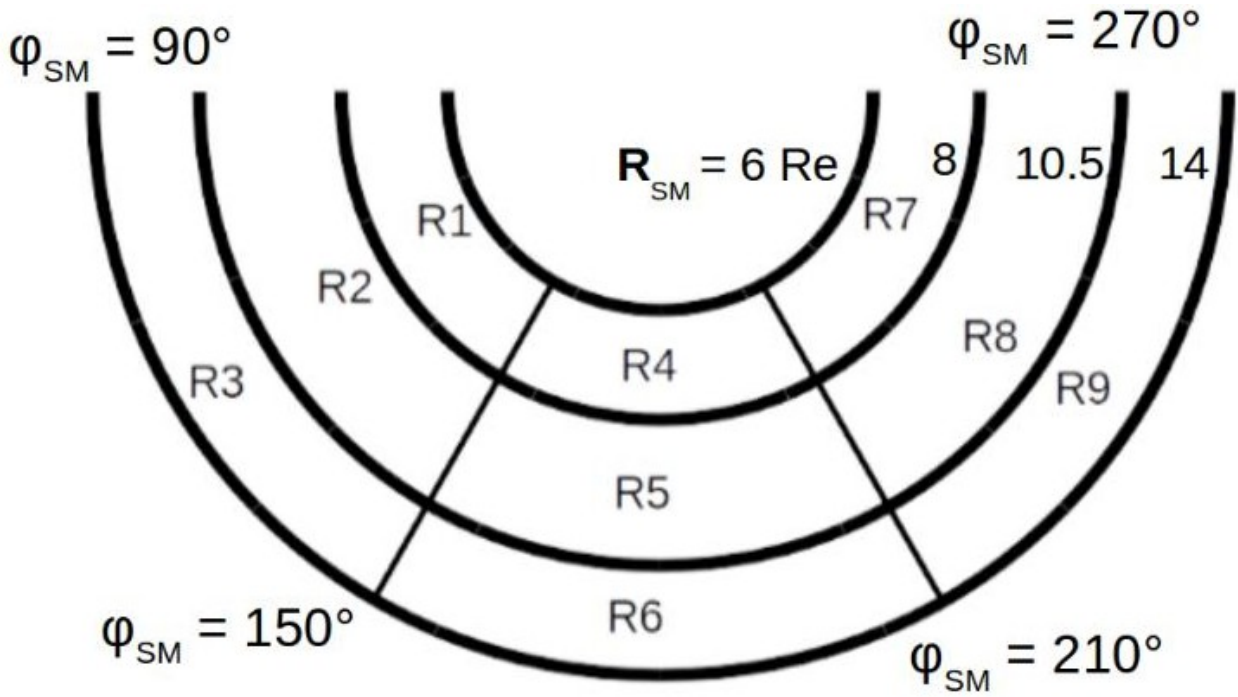
	Outputs ->			e flux 10 keV		e flux 31 keV		e flux 93 keV		p flux 34 keV		p flux 95 keV		p flux 140 keV	
	inputs (I)	# (i)	σ	vif	a	a*σ	a	a*σ	a	a*σ	a	a*σ	a	a*σ	a	a*σ
	const	0	0	0	-3.51	/	10.02	/	14.51	/	12.28	/	6.75	/	10.71	/
Solar wind	Vx 0.5/0.5	1	0.22	2.2	1.24	0.27	2.21	0.49	2.69	0.59	2.65	0.58	4.68	1.03	3.93	0.86
	N 0/0.5	2	0.63	1.92	0.27	0.17	-0.14	-0.09	-0.21	-0.13	0.03	0.02	0.01	0.01	0.26	0.16
	N 4/4	3	0.62	2.46	-0.04	-0.02	-0.12	-0.07	-0.23	-0.14	-0.10	-0.06	-0.14	-0.09	-0.08	-0.05
	N 16/8	4	0.61	1.71	-0.06	-0.04	-0.04	-0.02	-0.17	-0.10	-0.11	-0.07	-0.13	-0.08	-0.36	-0.22
	Pd 2/2	5	0.53	2.45	0.07	0.04	-0.11	-0.06	-0.18	-0.10	-0.03	-0.02	0.02	0.01	-0.15	-0.08
	Ekl 0.5/0.5	6	1.47	1.77	0.09	0.13	0.02	0.03	-0.01	-0.01	0.02	0.03	-0.02	-0.03	0.02	0.03
	EKL 2/2	7	1.19	2.32	0.23	0.27	0.20	0.24	0.17	0.20	0.24	0.29	0.16	0.19	0.07	0.08
	EKL 4/4	8	1.03	2.8	0.18	0.19	0.18	0.19	0.15	0.15	0.20	0.21	0.07	0.07	0.01	0.01
	EKL 8/8	9	0.89	2.44	0.11	0.10	0.10	0.09	0.16	0.14	0.09	0.08	-0.04	-0.04	-0.01	-0.01
	EKL 16/8	10	0.91	1.7	0.08	0.07	0.10	0.09	0.15	0.14	0.02	0.02	0.01	0.01	0.05	0.05
	NBL 0/0.5	11	1.32	2.2	-0.01	-0.01	-0.03	-0.04	-0.02	-0.03	0.00	0.00	0.01	0.01	-0.01	-0.01
	NBL 1/1	12	1.23	2.34	-0.13	-0.16	-0.16	-0.20	-0.12	-0.15	-0.13	-0.16	-0.15	-0.18	-0.07	-0.09
	NBL 4/4	13	1.02	2.17	-0.07	-0.07	-0.15	-0.15	-0.15	-0.15	-0.07	-0.07	-0.07	-0.07	-0.05	-0.05
	NBL 8/8	14	0.87	2.06	-0.06	-0.05	-0.10	-0.09	-0.11	-0.10	-0.13	-0.11	-0.17	-0.15	-0.09	-0.08
	NBL 16/8	15	0.9	1.51	0.01	0.01	-0.05	-0.05	-0.05	-0.05	-0.05	-0.05	-0.08	-0.07	-0.06	-0.05
SM	r	16	0.2	1.01	0.06	0.01	-6.07	-1.21	-9.44	-1.89	-7.16	-1.43	-11.66	-2.33	-11.89	-2.38
	Long	17	0.34	1.02	2.23	0.76	0.91	0.31	0.59	0.20	-0.05	-0.02	-0.35	-0.12	-0.28	-0.10
	num	\	\	\	232189		232013		227439		232186		185670		183442	
	CC	\	\	\	0.65		0.77		0.81		0.71		0.65		0.68	

	inputs (I)	# (i)	σ	vif	Ti_gmom a	a*σ	Te_gmom a	a*σ
	Outputs ->							
	const	0	\	\	7.83 /		-9.5 /	
	Vx 0.5/0.5	1	0.22	2.2	0.24	0.05	1.46	0.32
Solar wind	N 0/0.5	2	0.63	1.92	-0.03	-0.02	0.05	0.03
	N 4/4	3	0.62	2.46	-0.05	-0.03	-0.04	-0.02
	N 16/8	4	0.61	1.71	-0.03	-0.02	-0.08	-0.05
	Pd 2/2	5	0.53	2.45	0.07	0.04	0.08	0.04
	Ekl 0.5/0.5	6	1.47	1.77	0.01	0.01	0.06	0.09
	EKL 2/2	7	1.19	2.32	0.06	0.07	0.20	0.24
	EKL 4/4	8	1.03	2.8	0.06	0.06	0.11	0.11
	EKL 8/8	9	0.89	2.44	0.01	0.01	0.03	0.03
	EKL 16/8	10	0.91	1.7	-0.01	-0.01	0.04	0.04
	NBL 0/0.5	11	1.32	2.2	-0.01	-0.01	-0.03	-0.04
	NBL 1/1	12	1.23	2.34	-0.03	-0.04	-0.13	-0.16
	NBL 4/4	13	1.02	2.17	-0.01	-0.01	-0.09	-0.09
	NBL 8/8	14	0.87	2.06	-0.01	-0.01	-0.03	-0.03
	NBL 16/8	15	0.9	1.51	-0.01	-0.01	-0.01	-0.01
SM	r	16	0.2	1.01	0.3	0.06	0.29	0.06
	Long	17	0.34	1.02	-0.24	-0.08	1.43	0.49
	num	\	\	\	485900		489193	
	CC	\	\	\	0.48		0.66	

inputs del/avg hr.	Te gmom									Ti gmom								
inputs del/avg hr.	R1	R2	R3	R4	R5	R6	R7	R8	R9	R1	R2	R3	R4	R5	R6	R7	R8	R9
Vx 0.5/0.5	0.24	0.38	0.42	0.43	0.44	0.31	0.51	0.34	0.08	0.08	0.07	0.07	0.07	0.10	0.15	0.08	0.04	-0.03
N 0/0.5	-0.08	0.10	0.22	-0.01	0.05	-0.03	0.09	0.11	-0.12	0.02	-0.01	-0.04	0.03	0.02	0.00	0.04	0.06	-0.10
N 4/4	-0.14	-0.03	-0.01	0.06	0.04	0.02	0.07	-0.02	-0.05	-0.02	-0.01	-0.06	0.02	0.00	-0.04	-0.01	-0.02	-0.04
N 8/4	-0.09	0.00	0.02	-0.12	-0.01	-0.04	-0.10	-0.07	-0.04	-0.04	-0.01	-0.01	-0.03	0.01	-0.01	-0.02	0.02	-0.03
Pd 2/2	0.12	0.05	0.08	-0.02	0.01	0.03	-0.01	-0.03	0.03	0.04	0.02	0.01	0.02	0.04	0.04	0.01	0.01	0.07
Ekl 0.5/0.5	0.04	0.09	0.07	0.12	0.19	0.09	0.12	0.13	0.01	0.01	0.00	0.00	0.01	0.01	0.01	0.00	0.00	0.01
EKL 2/2	0.12	0.24	0.14	0.30	0.30	0.21	0.33	0.36	0.21	0.06	0.06	0.11	0.05	0.06	0.12	0.00	0.05	0.11
EKL 4/4	0.05	0.10	0.15	0.11	0.14	0.07	0.10	0.12	0.11	0.03	0.04	0.10	0.04	0.05	0.06	0.04	0.06	0.07
EKL 8/8	0.01	0.06	0.00	0.01	0.00	0.01	0.06	0.06	0.04	-0.01	0.01	0.01	0.00	0.00	-0.01	0.02	0.02	0.03
EKL 16/8	0.03	0.06	0.02	0.04	0.04	0.03	0.05	0.05	0.02	-0.01	-0.01	-0.01	-0.02	-0.03	-0.02	0.01	0.00	0.00
NBL 0/0.5	-0.04	-0.03	-0.04	-0.03	-0.07	-0.04	-0.07	-0.04	-0.04	-0.01	0.00	-0.01	-0.01	-0.01	-0.01	0.00	0.00	-0.01
NBL 1/1	-0.12	-0.14	-0.12	-0.25	-0.25	-0.16	-0.17	-0.16	-0.14	-0.01	-0.02	-0.05	-0.02	-0.04	-0.06	0.01	-0.01	-0.06
NBL 4/4	-0.10	-0.12	-0.08	-0.01	-0.07	-0.11	-0.13	-0.11	-0.08	-0.02	-0.03	-0.04	0.01	0.00	-0.03	-0.02	0.01	-0.02
NBL 8/8	-0.06	0.03	-0.04	-0.06	0.00	-0.02	-0.01	-0.06	-0.03	-0.01	-0.02	-0.03	-0.01	-0.01	-0.01	-0.02	-0.01	0.02
NBL 16/8	-0.04	-0.05	-0.04	0.03	-0.05	-0.03	-0.04	0.03	-0.01	-0.01	0.00	-0.01	-0.02	-0.01	-0.01	-0.01	0.02	-0.01
r	-0.87	0.21	0.61	-0.24	0.26	-0.08	0.02	0.18	-0.33	-0.07	0.12	-0.34	-0.04	0.09	-0.06	-0.11	0.16	-0.20
lon	0.02	0.62	0.69	0.54	0.55	0.33	-0.13	-0.18	-0.16	0.07	0.05	-0.02	-0.17	-0.15	-0.06	-0.15	-0.32	-0.30
num	38151	51911	72853	34620	43057	47946	38476	63681	98498	38153	51724	72436	33628	42302	47082	38479	63723	98373
CC	0.54	0.57	0.64	0.61	0.69	0.69	0.68	0.73	0.65	0.33	0.43	0.68	0.32	0.5	0.69	0.29	0.49	0.58

Row groups: "Solar wind" labels the rows from Vx 0.5/0.5 through NBL 16/8; "SM" labels the rows r and lon.

$\varphi_{SM} = 90°$

$\varphi_{SM} = 270°$

$\mathbf{R}_{SM} = 6$ Re

8   10.5   14

R7

R1

R2

R8

R3

R4

R9

R5

$\varphi_{SM} = 150°$

R6

$\varphi_{SM} = 210°$

Model performance for different iterations;
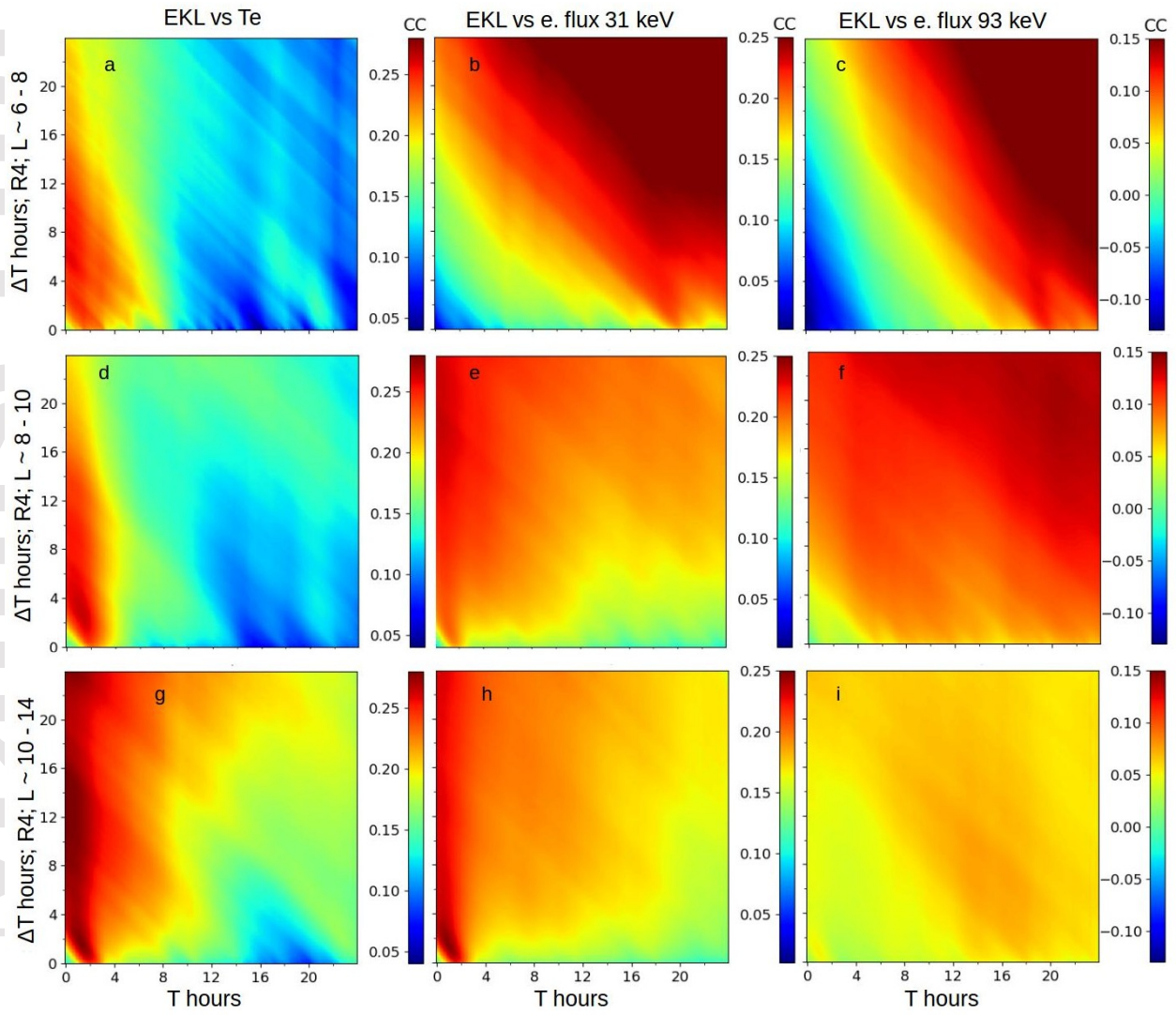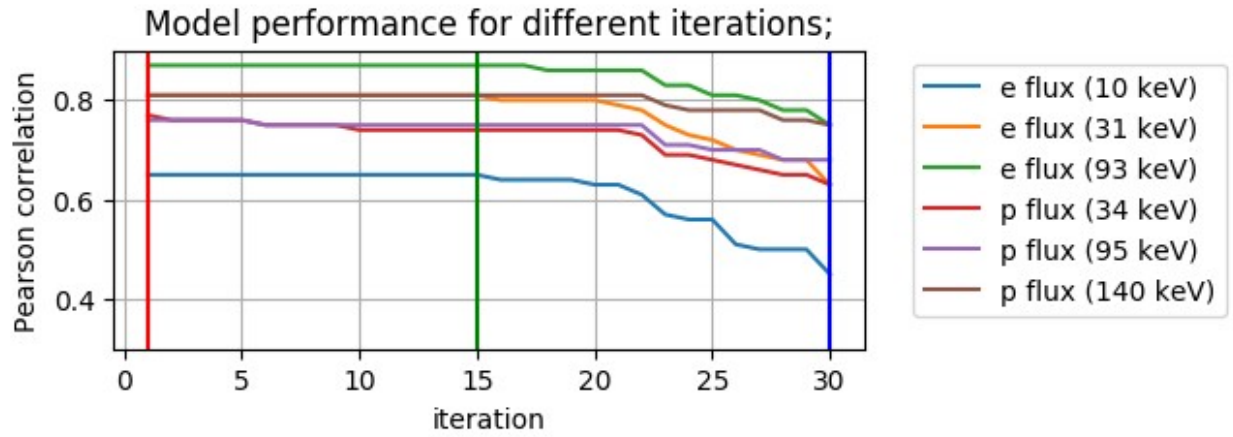
Predicted vs observed energy fluxes
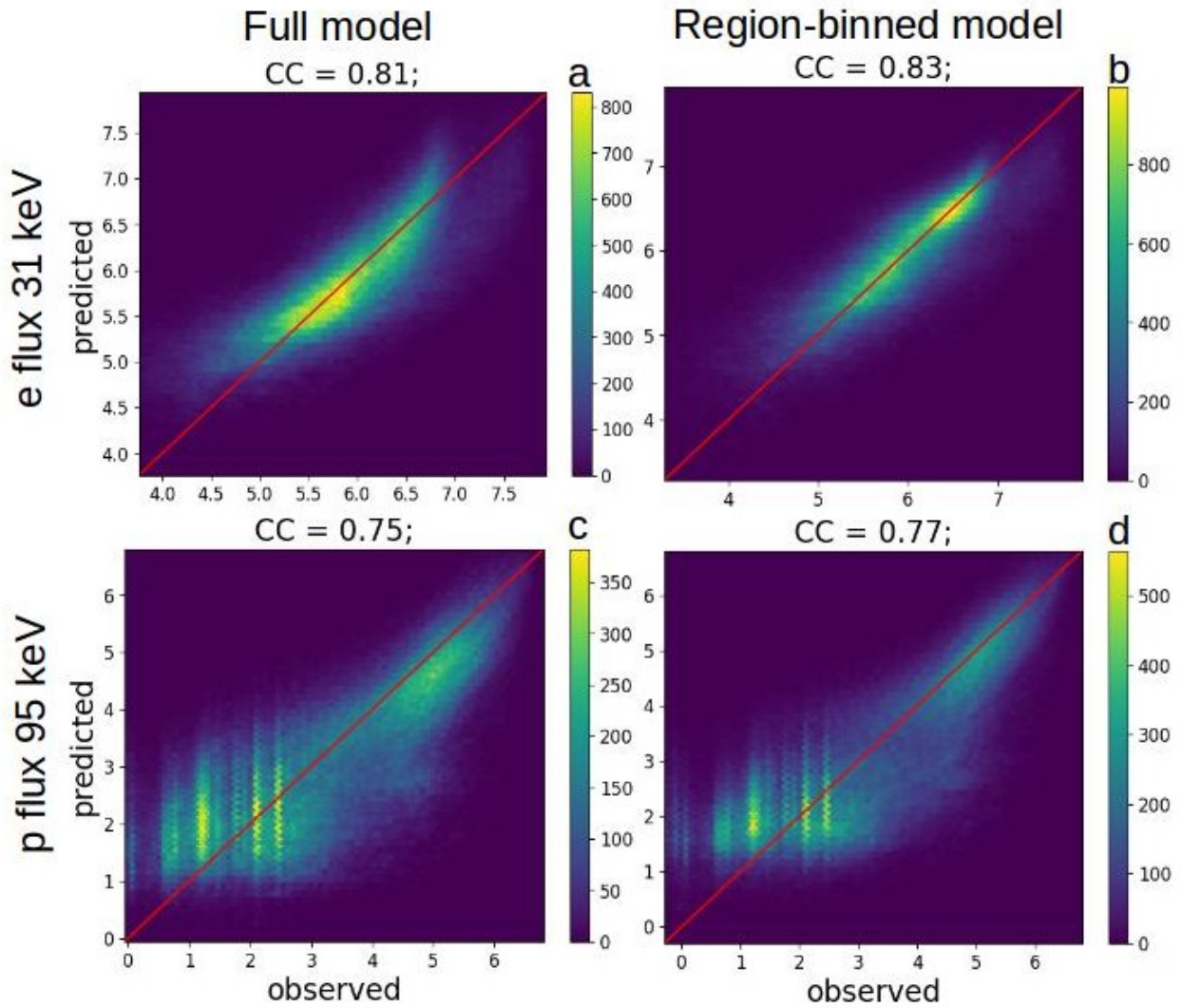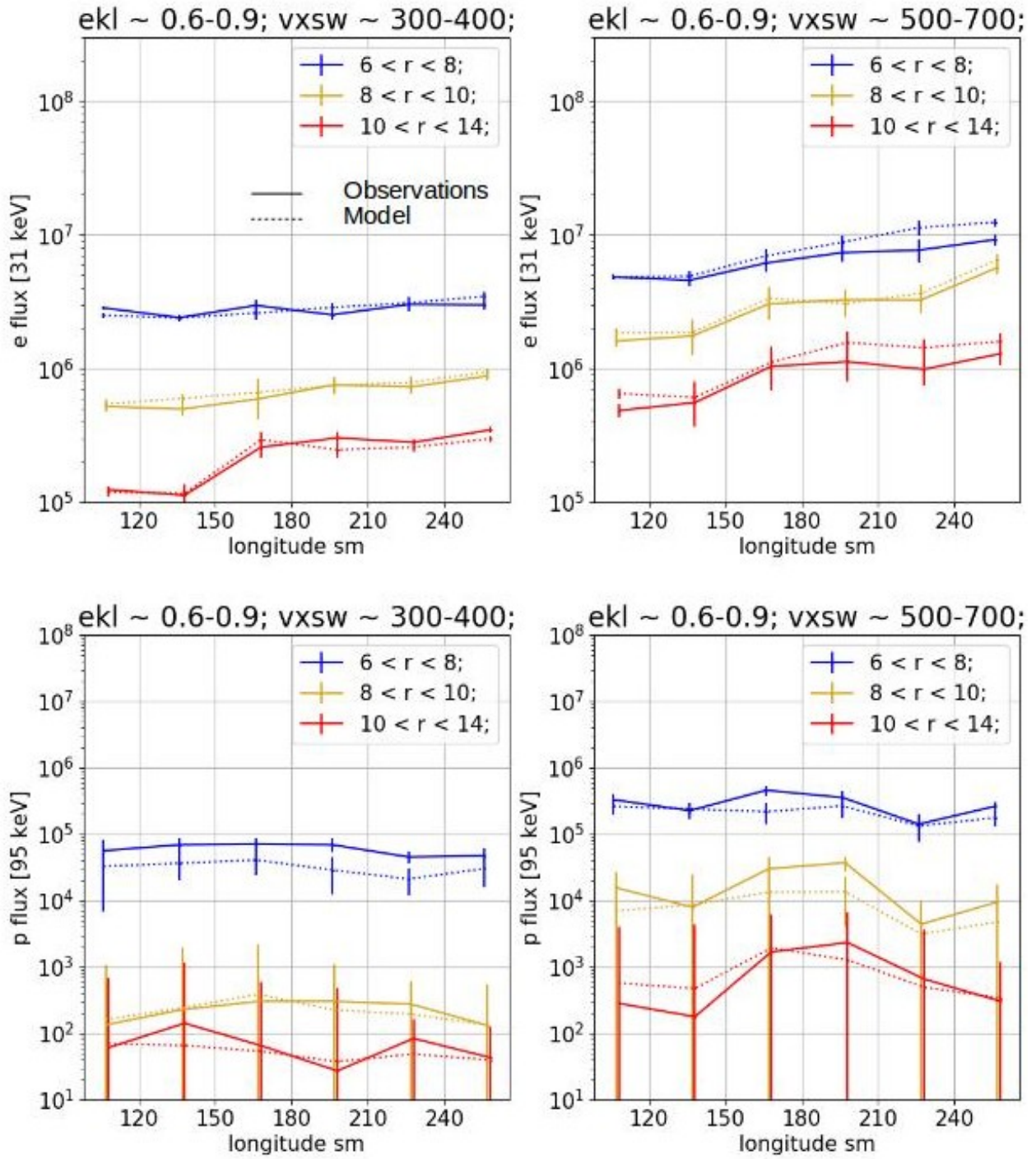
$$\log\left(eV*\left(s*cm^2*ster*eV\right)^{-1}\right)$$

Predicted vs observed electron energy fluxes $\log\left(eV*\left(s*cm^2*ster*eV\right)^{-1}\right)$

Full model

Region binned model

a — CC = 0.65;

b — CC = 0.71;

c — CC = 0.87;

d — CC = 0.89;

e flux 10 keV — predicted

e flux 93 keV — predicted
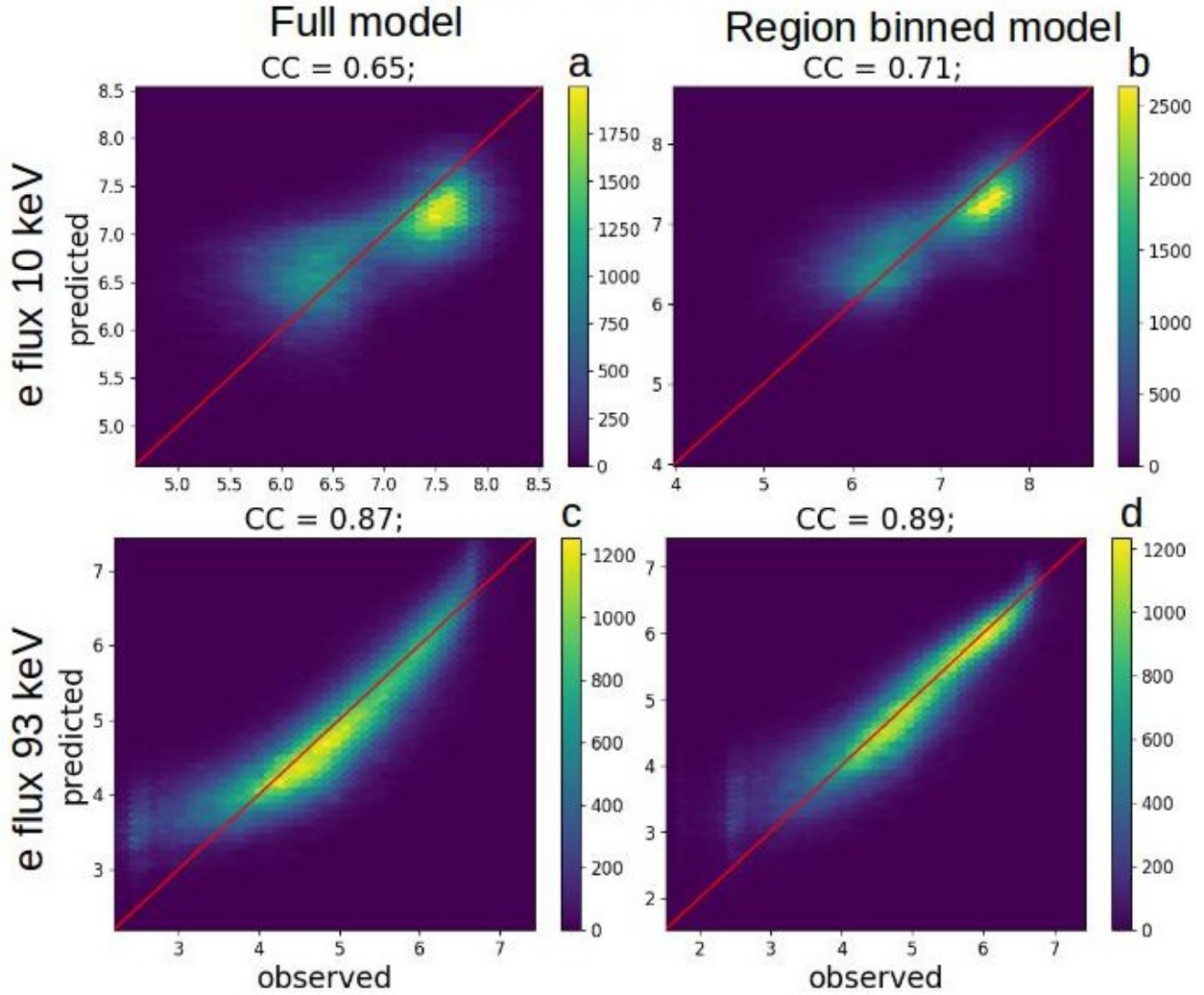
observed

Predicted vs observed proton energy fluxes $\log\left(eV * (s * cm^2 * ster * eV)^{-1}\right)$